The Ilopango Tierra Blanca Joven (TBJ) eruption, El Salvador: volcano-stratigraphy and physical characterization of the major Holocene event of Central America

Dario Pedrazzi[1], Ivan Sunye-Puchol[2], Gerardo Aguirre-Díaz[2], Antonio Costa[3], Victoria C. Smith[4], Matthieu Poret[3], Pablo Dávila-Harris[5], Daniel P. Miggins[6], Walter Hernández[7], Eduardo Gutiérrez[7]

[1] ICTJA, CSIC, Group of Volcanology, SIMGEO UB-CSIC, Institute of Earth Sciences Jaume Almera, Lluis Sole i Sabaris s/n, 08028 Barcelona, Spain

[2] Centro de Geociencias, Universidad Nacional Autónoma de México, Blvd. Juriquilla 3001, Campus UNAM, Querétaro, 76230, Mexico

[3] Istituto Nazionale di Geofisica e Vulcanologia, INGV-Bologna, Via Donato Creti, 12, 40100 Bologna, Italy.

[4] Research Laboratory for Archaeology and the History of Art University of Oxford 1-2 South Parks Road Oxford OX1 3TG, U.K.

[5] División de Geociencias Aplicadas, IPICYT, San Luis Potosí, 78216, Mexico.

[6] College of Earth, Ocean and Atmospheric Sciences, Oregon State University, 104 CEOAS Administration Building, 101 SW 26th St, Corvallis, OR 97331, EE. UU.

[7] Gerencia de Geología del Observatorio Ambiental, Ministerio de Medio Ambiente y Recursos Naturales MARN San Salvador, 76230, El Salvador

*Corresponding author (e-mail: dpedrazzi@ictja.csic.es)

Submitted to: JVGR

Abstract

The Ilopango caldera is the source of the large Tierra Blanca Joven (TBJ) eruption that occurred about 1.5 ka years ago, between ca. AD270 and AD535. The eruption dispersed volcanic ash over much of the present territory of El Salv.or, and pyroclastic density currents extended 40 km from the volcano. In this study, we document the physical characteristics of the deposits from all over El Salvador to further constrain the eruption processes and the intensity and magnitude of the different phases of the eruption. The succession of deposits generated by the TBJ eruption is made of 8 units. The eruption started with PDCs of hydromagmatic origin (Unit A_0), followed by fallout deposits (Units A and B) that are <15 cm thick and exposed in sections close to the Ilopango caldera (within 10-15 km). The eruption, then, transitioned into a regime that generated further PDCs (Units C-F), these range from dilute to dense and they filled the depressions near the Ilopango caldera with thicknesses up to 70 m. Deposits from the co-ignimbrite plume (Unit G) are the most widespread, the deposits are found in Guatemala, Honduras, Nicaragua, Costa Rica and the Pacific Ocean and cm-thick across El Salvador. Modelling of the deposits suggests that column heights were 29 km and 7 km for the first two fallout phases, and that the co-ignimbrite phoenix plume rose up to 49 km. Volumes estimated for the fallout units are 0.15, 0.8 and 16 km^3 dense rock equivalent (DRE) for Unit A, B and G respectively. The PDCs deposits volumes were estimated to be ~0.5, ~3.3, ~0.3 and ~9.1 km^3 DRE for Units C, D, E and F, respectively. The combined volume of TBJ deposits is ~30 km^3 DRE (~58 km^3 bulk rock), indicating that it was one of largest Holocene eruptions from Central America. This eruption occurred while Mayan populations were living in the region and it would have had a significant impact on the areas within tens of kilometres of the vent for many years to decades after the eruption.

Keywords: Pyroclastic Density Currents; Co-ignimbrite; Tephra fallout; Tephra dispersal modelling; Ilopango caldera

1. Introduction

Large caldera volcanoes pose a significant hazard to populations that surround them. In order to understand the likelihood and type of further activity it is key that the deposits of previous eruptions are well studied. This study focuses on the thick deposits of the Tierra Blanca Joven (TBJ) eruption from Ilopango Caldera, El Salvador.

Ilopango Caldera (IC; Fig. 1), located in El Salvador, is a 13 by 17 km volcano-tectonic structure filled by an intra-caldera lake (Mann et al., 2004), recently interpreted as a strike-slip caldera by Saxby et al. (2016). The IC belongs to the San Salvador Extensional Step-over in the central part of the country (SSES; Fig. 1b; Garibaldi et al. 2016), which is in turn part of the El Salvador Fault Zone-ESFZ (Montero and Dewey, 1982; Siebert and Simkin, 2002; La Femina et al., 2002; Corti et al., 2005; Turner et al., 2007). The IC was formed and shaped by various eruptions, and older (pre-57 ka) pyroclastic deposits are related to previous caldera collapse episodes (Lexa et al., 2011; Aguirre Díaz et al., 2017; Suñé-Puchol et al., 2019a,b). There are only a few publications that detail the eruptions in the last 57 ka, i.e. the TB4, TB3 and TB2 eruptions (Rose et al., 1999; Kutterolf et al., 2008a,b; Hernández, 2004; Hernández et al., 2012; Mann et al., 2004) and some recent studies have been carried out on the pre-57 ka ignimbrites of Ilopango (Hernández, 2004; Hernández et al., 2010; Lexa et al., 2011; Aguirre Díaz et al., 2017; Suñé-Puchol et al., 2019a,b). The latest studies focused on the eruption of a dacitic dome that formed the Islas Quemadas in Ilopango Lake (IQ; Fig. 1c) in 1879 (Richer et al., 2004), and a subaquatic eruption in this lake (Mann et al., 2004).

The last large explosive eruption of Ilopango volcano was the TBJ (*Tierra Blanca Joven* – white young earth), which is estimated to have erupted ~30 km^3 DRE of magma about 1.5ka years ago, between AD270 and AD535 (Dull et al., 2001; 2010). The TBJ was a cataclysmic eruption (Rolo et al., 2004) and is considered to be the largest in Central America since the ca. 84ka Los Chocoyos-Guatemala eruption (Dull et al., 2010). Outside of the zone of devastation by the TBJ eruption, there was a much larger area of prolonged depopulation (10-150 years) following the TBJ eruption (Dull et al., 2001).

Presently, the area around IC is densely populated with about 3,000,000 people living within 30 km of the caldera. The population density during most of the late Holocene in El Salvador has been the greatest of any mainland country in the Americas (Daugherty 1969; Denevan 1992; Lovell and Lutz 1995; Wilkie and Ortega 1997). Since the last eruption was in AD1879, IC is still considered active and, it poses a major risk for El Salvador and neighbouring countries. In order to contribute to the hazard assessment at IC, we conducted a detailed field mapping to further investigate the TBJ deposits with the aim of building on the previous work and accurately reconstructing the eruption sequence.

There have been several publications about the TBJ eruption deposits. They were first documented by Williams and Meyer Abich (1955) and called "white earth" due to their peculiar white colour, although they were thought to originate from San Salvador Volcano. Further studies of IC deposits were carried out by the German Geological Mission (MGA) whilst they completed the 1:500,000 scale El Salvador Geological Map (Weber et al., 1974). They defined IC and divided the proximal deposits into Units s4 (TBJ deposits) and s3'a (TB4, TB3 and TB2 eruptions) as part of the San Salvador Formation. Later, Hart (1981) worked on the detailed stratigraphy of the TBJ deposits and identified two important eruptive stages; T1 and T2, whose products are subdivided into six units and associated with different eruptive phases. Subsequently, Hart and Steen-McIntire (1983) described the stratigraphy and distribution of the TBJ tephra and Vallance and Houghton (1998) revised the stratigraphy of Hart and Steen-McIntire (1983) and labelled the stratigraphic units, characterizing them lithologically and refining associated eruptive processes. Recent works on TBJ by Hernández (2004) identified new ignimbrites (Alpha, Beta, and Gray) and detailed the characteristics of each unit in more detail.

Despite all this studies, a detailed stratigraphic survey including mapping and reconstruction of eruptive dynamics was still lacking. This study presents new field descriptions, petrographic observations, major element glass geochemistry, granulometric data for the TBJ deposits, and uses these data to further understand transport/depositional mechanisms and the corresponding eruption dynamics of the TBJ eruption. Moreover, the physical parameters of the eruption were determined, including the total erupted mass, the height of the eruptive columns, the emission rate, the duration of the eruption, and, above all, reconstruct the distribution of the TBJ deposit using models and field observations. In particular, the stratigraphic and granulometric data obtained in the field were used to model the distribution of the TBJ tephra, including the dispersion of the finest ash that covered vast areas (thousands of km^2).

2. Geological Setting

Central America and El Salvador geodynamic and geology

El Salvador is located in North Central America, on the Pacific margin of the Caribbean Plate (Fig. 1a). To the north, this plate interacts with the North American plate with a relative velocity between plates of 19 mm/year (DeMets et al., 2000; Guzmán - Speziale et al., 2005; Funk et al., 2009). Towards the west of El Salvador, the relatively young Cocos Plate (<25 Ma; Protti et al., 1995; Barckhausen et al., 2001) subducts towards the NE under the Caribbean plate along the Middle America Trench, at a speed of 73-85 mm/year (Dixon, 1993; De Mets, 2001).

The highest rate of continental tectonic deformation in El Salvador occurs in the El Salvador Fault Zone (ESFZ), a narrow E-W zone of right lateral faulting connected by pull-aparts, that extends for more than 150 km (Martínez - Díaz et al., 2004; Fig. 1a) from Guatemala, where it is known as the Jalpatagua Fault (JF), to the Nicaragua Depression (ND) (Canora et al., 2012). These faults are sub-parallel and affect volcanic deposits and volcanic rocks of Pleistocene-Holocene age (Corti et al., 2005). Geological and seismological analyses suggest that ESFZ is not laterally continuous and it has been subdivided into different sections (Martínez - Díaz et al., 2004; Corti et al., 2005).

The chain of volcanoes along the Central American Volcanic Arc (CAVA; Fig. 1a) has been developing since the Tertiary (De Mets, 2001; Mann, 2007; Carr et al., 2007) and is part of the Pacific Ring of Fire (Simkin and Siebert, 1994; Carr et al., 2007; Saxby et al., 2016). The CAVA extends for more than 1,000 km from the southeast of Mexico to the central valley of Costa Rica and defines an abrupt continental volcanic front located between 165-190 km from the Middle America Trench (Fig. 1a). Volcanoes of Panama are excluded from the CAVA as they are associated with the subduction of the Nazca Plate below the Caribbean, which makes them distinct in composition and activity relative to those in the CAVA (Carr et al., 2007).

Volcanism of the Volcanic Arc of El Salvador (VAES) constitutes one of the most active segments of the CAVA. VAES includes 21 active volcanoes, three of which have erupted in the last century (Santa Ana-SA, Izalco-I, San Salvador-SS and San Miguel-SM, Fig. 1b; Siebert and Simkin, 2002). Deposits from these volcanoes, together with volcanic rocks of ages ranging from the Cenozoic to the present, constitute most of the geology of El Salvador (Fig. 1b).

Ilopango Caldera

The IC (Fig. 1c) is located less than 10 km from San Salvador City and it forms part of the same eruptive lineament as the San Salvador and San Vicente volcanoes (Fig. 1b). IC is located directly above faults in the San Salvador and San Vicente ESFZ segments within the San Salvador Pull-Apart (SSPA; Garibaldi et al., 2016), which is a tectonic structure-oriented NW-SE, with right trans-tensive dynamics, parallel to the Mesoamerican trench. The transforming faults of the graben / pull-apart seem to control the morphology of IC, its formation and its volcanic eruptions (Soefield, 2004; Suñe-Puchol et al., 2019a), as described for other Graben Calderas (Aguirre-Díaz, 2008). Several authors, in their study of volcanism in southern El Salvador, noticed that the IC was a volcanic-tectonic depression controlled by the faults of an ancient graben (Williams and Meyer-Abich, 1955; Golombek and Carr, 1978; Hutton and Reavy, 1992; Soefield 2004; Aguirre-Díaz et al., 2015, 2016, 2017). Recently, Saxby et al. (2016) interpreted IC as a strike-slip caldera. IC was the result of several collapses associated to large explosive ignimbrite-forming eruptions (Suñé-Puchol et al., 2019a,b) as previously suggested by Williams and Meyer-Abich (1955). The topographic edge of IC has several semicircular bays (Fig. 1c), which are evidence for multiple collapse events (Lexa et al., 2011).

3. Methods

Field mapping was carried out over an area of about 20,000 km^2, across El Salvador to reconstruct the stratigraphy of the TBJ deposits and the stratigraphic relationships with other eruptive deposits. The characteristics of the deposits were recorded including grading, colour, sorting, apparent component content (juvenile and lithic fragments), and primary sedimentary structures. The nomenclature used in this study for the bed thickness, grain size and sorting of the pyroclastic deposits follows that proposed by Sohn and Chough (1989). The classification of the primary volcaniclastic deposits follows White and Houghton (2006) and the nomenclature for volcanic stratigraphy is based on Martí et al. (2018), adopting the same criteria as Suñé-Puchol et al. (2019a,b) for the previous Ilopango eruptions. A total of 82 stratigraphic sections were measured, but we focus here on 21 outcrops that we consider representative of the whole succession, and its spatial variations and preservation of deposits.

The geographical coordinates of the locations, stratigraphic sections and sampling points were recorded using a portable Garmin Dakota-20 GPS (precision of ~3 m) and quoted on the UTM projection Datum: D_WGS_1984, zone 16N. All this local information is reported in Supplementary Material 1. All the georeferenced data were managed and processed using the open source software Quantum GIS (Las Palmas; https://www.qgis.org/en/site/).

Thicknesses of the deposits and specific units were measured to create a database (see Supplementary Material 1) for tephra dispersal simulations (Macedonio et al., 2005). Tephra dispersal from virtual sources in an eruption column was simulated using the HAZMAP model, which solves equations for advection, diffusion and sedimentation of tephra particles in two dimensions (Macedonio et al., 2005). We followed an approach similar to Matthews et al. (2012) but used the Total Grain Size Distributions (TGSDs) (Bonadonna and Houghton, 2005) phases determined through the Voronoi Tessellation method, that we estimated for the different phases using data collected in this study. The granulometry data used to generate the TGSDs are available in Supplementary Material 2. Isopach maps were generated by modelling the ash deposition in terms of mass loading (kg/m^2) and these were converted into thicknesses using a bulk density of 1,000 kg/m^3. In addition to the volumes, the solution of the inverse problem (Costa et al., 2009; Matthews et al., 2012) allowed us to estimate column heights, from which, by using the results of Mastin et al. (2009) and Bonadonna and Costa (2013), we assessed the corresponding Mass Eruption Rates (MER) for each unit. The volume estimations of the PDCs units were determined using the Delaunay triangulation method (Macedonio and Pareschi, 1991) that is particularly suitable for the reconstruction of volume between geological horizons and the interpolation of bivariate data, when function values are available at irregularly-spaced data points, as in the case of geological outcrops.

A binocular microscope was used to determine the main petrographic and textural characteristics of the juvenile components. In addition, petrographic analyses were carried out in order to identify the mineralogy and general composition of the studied deposits. Thin sections were produced at Wagner Petrographic LLC, a professional company of Lindon, Utah (USA).

Granulometric analyses were performed at the MARN (Ministerio de Medio Ambiente y Recursos Naturales) facilities of El Salvador Government and the Physical Volcanology Laboratory of Centro de Geociencias, UNAM in Juriquilla-Querétaro (Mexico). Representative levels of each stratigraphic unit were sampled and analysed (141 samples in total; Fig. 2 and Supplementary material 2) for grain-size distribution and componentry. Grain-size analysis were performed by dry sieving at 1 phi (Φ) intervals through sieves with aperture sizes ranging from 64 to 0.25 mm (−6 Φ to 3 Φ, where $\Phi = -\log_2 d$ with d is the diameter in mm) and by wet sieving through a MicroTec Analisette22 Fritsch from 0.125 mm to less than 0.01 mm (4 Φ to >10 Φ). The weight percentages of the sieved fractions were calculated and then plotted as cumulative curves to give grain-size distribution. All data from grain-size analysis are reported in Supplementary Material 3 and 4. The proportion of juveniles from −5Φ to 0Φ was defined by hand picking and from 0 Φ to 2 Φ using a binocular microscope and image analysis techniques (e.g. ImageJ software; https://imagej.nih.gov/ij/). This point-counting method allows identifying the different components of each particle-size class using binocular microscope pictures. Modal proportions of juvenile pumice and accidental lithic fragments are reported in Supplementary Material 5.

Whole rock pumice geochemical analyses for major elements, trace and rare earth-elements (REE) (Table 2) were measured at the CGEO LEI laboratory (trace and REE, with an ICP-MS) and at Instituto de Geología of UNAM (major and trace elements, X *RIGAKU ZSX Primus II* spectrometer), following standard sample preparation and analytical techniques (Bernal and Lozano-Santacruz, 2005).

Electron probe X-ray microanalysis for mineralogy was performed using a JEOL JXA-8230 electron microprobe at the Scientific and Technological Centers (Universitat de Barcelona). Wavelength-dispersive analyses of silicates were conducted using a 20 kV accelerating voltage and 15 nA current and with a focused beam. Glasses were analysed using a 6 nA current with a defocused 5-10 micron spot. Counting times were 10 s peak and 10 s background. A range of natural and synthetic standards was used for calibration. The correction model XPP was used to convert X-ray intensity ratios into concentrations. Data are included in Supplementary Material 6.

The major element compositions of the matrix glass of the TBJ were determined using wavelength-dispersive electron probe microanalysis (EPMA) in the Research Laboratory for Archaeology and the History of Art at the University of Oxford. Analyses were carried out on samples from all units, A to G, and distal deposits located up to 130 km from the caldera. The EPMA of the TBJ glasses were acquired using an accelerating voltage of 15 kV, beam current of 6 nA, and 10-μm-diameter beam. The count times on peak were: 30 s for Si, Al, Fe, Ca, K and Ti; 50 s for Cl and Mn; 60 s for P; and 12 s for Na, and background counts were collected for the same amount of time but split to positions either side of the peak. The PAP absorption correction method was used for quantification and the oxide compositions quoted assume stoichiometry. The electron probe was calibrated for each element using well-characterized mineral standards, which was verified by analysing MPI-DING reference glasses (Jochum et al., 2006). These MPI-DING glasses were used as secondary standards during each analytical run, and this data is included in the Supplementary Material 7 as they demonstrate the accuracy and precision of the TBJ datasets. All the glass analyses presented have been normalized to 100% to account for variable hydration and allow different samples to be compared, and all the raw compositional data can be accessed in Table 3.

4. Characteristics of the pyroclastic succession

Proximal TBJ member products (0-10 km from the caldera) are exposed inside and close to the caldera with a maximum observed thickness of ~60 meters (Supp Material 1). The TBJ member can be divided in 8 units that were labelled alphabetically from base to top (A_0-G; Fig. 2). Due to differences in dispersal patterns, lateral facies variations and surface erosion, the complete stratigraphy was reconstructed from a large number of individual outcrops. Simplified stratigraphic logs of 21 localities are shown in Fig. 2. They were arranged from west (left) to east (right) and from south to north, across El Salvador in order to show how single units correlate with each other. A composite section is also shown in figure 2 and illustrates the general stratigraphy of the TBJ member. The TBJ member consists of initial pumice lapilli-supported grain deposits and later of several units made of a coarse and fine ash, matrix-supported massive deposits with pumice lapilli and lithics interbedded with laminated levels of lapilli (i.e. ILO 18 and ILO22; Fig. 2). All these deposits were mapped across several dozens of km from the caldera rim. The medial succession can be observed up to 30-40 km from the caldera rim, where the best exposures are found on the southern slopes of IC (i.e. ILO 8 and ILO130; Fig. 2). The last unit, which comprises massive fine-grained deposits, is observed in medial exposures and distal ones that are more than 100 km from the caldera (i.e. ILO289 and ILO302; Fig. 2). Deposits from the TBJ eruption are characterized as being white soft and easily erodible, generating "badlands" type scarps (Šebesta, 2007). Most of the San Salvador Metropolitan Area (Fig. 1c) has been built on the TBJ tephra deposits.

Unit A_0

A_0 is the first unit in the TBJ succession of deposits (stratigraphic log 22 in Fig. 2), which is observed in medial (10-40 km from the vent) outcrops mainly to the south of the caldera. Thickness ranges from 2 to 4 cm (Supplementary Material 1) and the deposits are characterized by poorly-sorted, thinly bedded or laminated, moist beds of rounded dense, glassy coarse and fine pumice ash with accidental lithic fragments. The deposit usually rests directly upon a paleosol or older, weathered pre-caldera lavas. At the outcrop scale, there are lateral variations in the thickness and number of beds, with pinch and swell structures and locally erosive basal contacts (Figs. 3a,b).

Unit A

Unit A (stratigraphic logs 22, 172, 247, 291 in Fig. 2) outcrops in different points around IC, but mainly in the eastern and southern sectors at medial locations. It shows thicknesses from 3 to 14 cm (Supplementary Material 1) and is characterized by massive well-sorted thin to medium coarse angular pumice ash beds (Figs. 3a,b) with ash-sized lithic fragments. A planar contact separates it from the underlying Unit A_0.

Unit B

Unit B (stratigraphic logs 18, 22, 38, 49, 172, 247, 291 in Fig. 2) is characterized by moderately to poorly-sorted, massive thin beds of angular pumice lapilli and lithics with no ash (Fig. 3c). Thicknesses vary from 1 to ~5 cm (Supplementary Material 1). This deposit shows sometimes yellowish colour due to the pigmentation and cementing of iron oxides by contact with the underlying paleosol. It appears in several outcrops at proximal and medial locations.

Unit C

Unit C (stratigraphic logs 8, 18, 22, 49, 247 in Fig. 2) is only preserved at a few outcrops in proximal and medial locations. It has a peculiar grey-yellowish colour (Fig.

3a) and is a well-sorted, matrix-supported deposit with light stratification of pumice fragments with scattered accretionary lapilli and hydrothermally altered lithics. Observed thicknesses range from a few cm up to 10 m in some depressions (Supplementary Material 1).

Unit D

Well-sorted, massive, lithic-poor ash rich deposit (Fig 3d). Unit D outcrops at proximal and medial locations (stratigraphic log 8, 18, 22, 28, 38, 49, 172, 247, 291, 293 in Fig. 2). The intermediate and distal (>40 km from the caldera) facies of this unit is quite unconsolidated with a fine ash matrix and dispersed pumice juvenile fragments (Fig. 3ei) and with slight variations between one horizon and another. At proximal locations the deposits are more cemented with a coarse ash matrix and containing beds that show a strong enrichment of millimetric accretionary lapilli (Fig. 3eii). At some outcrops, the deposit shows planar stratification. The maximum measured thickness of the Unit D is about 8 m (Supplementary Material 1).

Unit E

Unit E consists of doublets of thin to medium thick massive and laminated beds of rounded lapilli and coarse ash pumice (Figs. 3d,f). The unit outcrops at proximal and medial locations from the caldera (stratigraphic logs 8, 18, 22, 28, 49, 172, 247, 293 in Fig. 2). It represents a good stratigraphic marker of the TBJ eruption and to differentiate between Units D and F (Fig. 3d). The massive deposits are light coloured and composed of unconsolidated thick ash with pumice thin lapilli and lithics. The laminated deposits constitute very fine, well-sorted ash, that is light brown and dark brown when wet. It is commonly quite consolidated and rich in glass fragments and crystals. Locally, these deposits show folding that is characteristic of soft sediments (Fig. 3g). The maximum measured thickness is 1 m (Supplementary Material 1).

Unit F

Unit F is composed of chaotic, massive, poorly-sorted, non-welded, light-coloured to light beige (Fig. 3d) with thickness up to about 60-70 m thick (Supplementary Material 1). Unit F outcrops at both proximal and medial locations (stratigraphic logs 8, 18, 22, 28, 32, 33, 46, 49, 51, 130, 165, 169, 172, 247, 286, 293 in Fig. 2) and found up to 40 km from the caldera. To the north, the deposits extend away from the caldera for at least ~35 km and outcrop close to Cerrón Grande (Fig. 2). To the west, deposits cover part of San Salvador Volcano (Fig. 2), reaching a maximum height of 930 m (1,740 m a.s.l.). Deposits were also found close to the Municipality of Colón

(Fig. 2), where they achieve a distance of ~40 km. Towards the southern part (Balsamo Cordillera; Fig. 2), deposits outcrop along the old channels of rivers and streams reaching distances of more than 30 km. East of IC, Unit F was recognized up to 30-35 km away, close to the San Vicente Volcano (Fig. 2). The deposits in the proximal outcrops show a coarse ash matrix with abundant centimetre- and decimetre-sized pumice and lithic fragments (Figs. 3h,i). Visibly mingled pumice with dark to light grey bands within the white pumice are found in unit F at very proximal sites within the caldera, e.g. ILO-32 (Fig 3h). The abundance of mingled clasts at this site is ~5-10% and the clasts range from around 5 to 20 cm in length.

Some decimetre-sized lithic-rich beds are observed close to the caldera edge (Fig. 3j). Medial outcrops show the same massive, lithic-rich deposits with a fine ash matrix, and lithic and juvenile pumice up to few centimetres in size (Fig. 3k). Most of the outcrops show a lower layer with higher particle concentrations. Degassing pipes are seen in this unit at some outcrops (Fig. 3l). In some cases, Unit F is found directly above Unit D or with a reworked lower part (Fig. 3m).

Unit G

It is an unconsolidated, massive, well-sorted, coarse to fine ash deposit with millimetre-sized accretionary lapilli (Fig. 3n). In some outcrops, a slight stratification is observed, with a transitional contact with Unit F below. Deposits were described mainly at medial and distal outcrops (stratigraphic logs 22, 46, 49, 113, 130, 165, 169, 172, 289, 302 in Fig. 2) and found up to 100 km from the vent (Fig. 3o). Maximum measured thicknesses are ~6 m (Supplementary Material 1).

5. Physical parameters

Grain-size distribution

Data from Supplementary Material 3 was plotted in Supplementary Material 4 in order to show variation of TBJ grain-size at proximal (0-10 km), medial (10-40 km) and distal locations (>40 km) from IC. Data include Medium Diameter (MdΦ), Sorting (σΦ) and Skewness (αΦ) parameters (Supplementary Material 4a-4f) as well as F1 [wt.% <1 mm diameter (0Φ)] and F2 [wt.% <1/16 mm diameter (4Φ)] (Supplementary Material 4g-i). Granulometric data of the local distributions characterized up to phi 10 were used to reconstruct the Total Grain Size Distributions (Fig. 4).

Figures j-ac of Supplementary Material 4 illustrate the grain-size distribution of the TBJ samples depending on distance from the caldera. Both A_0 and A samples show a bimodal trend. Conversely, samples from Unit A are characterized by a unimodal trend. No proximal and distal samples were found for both Units A_0 and A. Only two samples from Unit B were collected at proximal locations, and only one of the two samples shows a unimodal trend. Medial samples from Unit B seem no show a clear relationship between distance and grain size trend similarly to the only sample from a distal outcrop that only shows a slight shift to finer classes. Two samples from Unit C at proximal locations show a polymodal trend, similarly to the ones at medial outcrops. Only one sample was collected from distal outcrops showing a shift towards finer classes. However, unlike Unit C, samples from Unit D at proximal and medial outcrops have a clear polymodal trend. Therefore not a clear relationship between distance and grain size trend was observed for sample from this unit. Only one distal sample from Unit D indicates a shift towards finer classes similar to the samples from Unit C. Two proximal samples from Unit E show different tendencies with a unimodal trend but towards coarser and finer classes. The same is observed at medial distance. Only one distal outcrop from Unit E was found in the field. It shows a clear shift towards finer classes. Proximal and medial samples from Unit F show a polymodal trend with coarser classes being more representative. Distal samples from Unit F seem to show a slight bimodal trend without any substantial change in the granulometrical distribution. Only one sample from Unit G was collected at one proximal outcrop. Medial and distal samples from Unit G are characterized by a bimodal trend.

Componentry analysis

Componentry of individual beds is presented in Fig. 2 and Supplementary Material 5. The modal proportions of juvenile pumice and accidental lithic fragments (mafic clasts and pre-TBJ eruption ignimbrites) are given for each grain-size fraction (or class) until 2Φ and their distribution among grain-size fractions, as well as units is not costant. Unit A_0, which is only present at few scattered medial outcrops, has a lithic content of ~8-8.5%. The following Unit A shows variable values from ~10-11% up to ~22-23% at medial locations. Unit B, at medial locations, shows values between ~15 and ~19% up to 28%. At distal outcrops, lithics are ~12%. Unit C at proximal outcrops contains total lithic values of ~9%. Medial outcrops are characterised by lithic values of ~5-8.5%. Unit D shows a constant lithic content from proximal to distal outcrops with values ~1-4%. Unit E shows values comprised between ~8% and ~16% although several samples show a considerable decrease with only lithics of ~3%. Unit F at proximal outcrops shows values ~15% of lithics whilst at medial outcrops values are generally around 5-15%. Unit G is characterised by lithics values at medial and distal outcrops of ~1-3%.

Product distribution and volume of the different eruptive phases

The distribution of outcrops and the thickness data (reported in the Supplementary Material 1) from each unit is shown in Fig. 5. Combining these field observations and dispersal models for each phase, we estimate the corresponding mass of erupted material (in terms of DRE) and intensity (in terms of discharge rate).

Concerning the fallout units, which includes Units A and B from sustained eruption columns, and G from a co-ignimbrite plume, we computed the tephra transport and sedimentation by solving an inverse problem (Pfeiffer et al., 2005; Costa et al., 2009) using the tephra dispersal model Hazmap (Macedonio et al., 2005). The results are summarized in Table 1, where the Total Erupted Mass (TEM), the column height, maximum wind intensity, and other physical parameters are reported for the different units. Furthermore, for Unit A we estimated a TEM of ~3.5×10^{11} kg (i.e. 0.15 km^3 DRE assuming a constant magma density of 2,300 kg/m^3), and an eruptive column height of ~29 km, corresponding MER of < ~10^8 kg/s (Bonadonna and Costa, 2013). TEM for Unit B is of ~2×10^{12} kg (i.e. 0.8 km^3 DRE), with an eruptive column height of ~7 km, corresponding MER of ~10^5-10^6 kg/s (Bonadonna and Costa, 2013). For the fallout unit G from the co-ignimbrite column, we adopted a first order approach similar to Matthews et al. (2012). Results of the inverse problem for the co-ignimbrite phase suggest a TEM of ~4×10^{13} kg (i.e. 16 km^3 DRE) with a co-ignimbrite plume that reached a height of ~49 km (corresponding to a MER of ~10^{10} kg/s). For the co-ignimbrite plume the source of ash is not “point source” but rise from all the surface of ignimbrite sheet, which can have a radius >30-50 km (Costa et al., 2018). For this reason, the validity of the tephra dispersal model, which assumes virtual sources along an eruption column, is not fully appropriate for points at distances smaller than 30-50 km and simulation results should be considered simply as model extrapolations. However, in our case most of the available outcrops were at larger distances (see Supplementary Material 1). The individual grain-size distributions of the samples of each unit at several locations (Fig. 2 and Supplementary Material 2) were used to generate the TGSDs (Total Grain Size Distributions) reported in Figure 4. These TGSDs were estimated using the Voronoi tessellation method of Bonadonna and Houghton (2005). For the sake of comparison, the volumes of Units A, B, and G were also assessed by adopting empirical integrations of the deposit thinning (Bonadonna and Costa, 2012).

The dispersal of the different units as isopachs is shown in Fig. 5. From these maps, we can see that Units A (Fig. 5a) and B (Fig. 5b) were mainly dispersed to the west and west-south-west areas, respectively. In contrast, Unit G (Fig. 5g) was dispersed towards the south by weak winds.

Taking into account that PDC of Unit F had a runout distance of ~50 km (Fig. 5f), from the results of Costa et al. (2018) we can estimate a MER of order of 10^{10} kg/s, which is consistent with the value estimated for the co-ignimbrite phase (Unit G) on the basis of the height of the co-ignimbrite plume (see Table 1). The volume of PDC Units C, D, and F were calculated using the Delaunay triangulation method (Macedonio and Pareschi, 1991), which is, as mentioned in the Methods Section, suitable for assessing the volume between geological horizons from irregularly-spaced data points. We obtained the following volume estimations:

1. ~0.7 km^3 (i.e. ~0.5 km^3 DRE) for Unit C;
2. ~5.0 km^3 (i.e. ~3.3 km^3 DRE) for Unit D;
3. ~0.5 km^3 (i.e. ~0.3 km^3 DRE) for Unit E;
4. ~14 km^3 (i.e. ~9.1 km^3 DRE) for Unit F.

DRE volumes were calculated using an assumed deposit density of ~1,500 kg/m^3 (Quane and Rusell, 2005) and a magma density of 2,300 kg/m^3. These volumes indicate that 30 km^3 of magma was ejected during the TBJ eruption.

6. Petrography, geochemistry and glass compositions of the TBJ deposits

Pumice clasts from the TBJ units are moderately crystal-rich (up to 10-15%) and highly vesicular. Mineralogy assemblage consists of 70-75% euhedral to subhedral plagioclase (andesine and labradorite; Figs. 6a-d and Fig. 7a), about 20% of magnesio-hornblende (Figs. 6a,b,e,f and 7b), and 10 vol.% of crystal content is made of pyroxene (Figs. 6g,h and 7c,d), Fe-Ti oxides and apatite. Plagioclase crystals often have sieve-textured cores and contain apatite inclusions, Fe-Ti oxides and clinopyroxene (Figs. 6a-d). The hornblende crystals (Figs. 6e, f) have pristine rims with abundant inclusions of apatite (Fig. 6a) and orthopyroxene.

Whole-rock compositions of the TBJ pumices are dacitic to rhyolitic (Fig. 8a and Table 2), and glass compositions are typically rhyolitic with the exception of mingled pumices found in the upper sequence (Unit F; see above) that extend to basalt

(Fig. 8a). The glass compositions were determined for individual shards using an electron microprobe from samples through the entire succession of deposits, and from both proximal and distal sites. Excluding the rare mingled clasts in Unit F, other deposits display homogenous, rhyolitic major element compositions with SiO_2=75.3-78.1 wt.%, Al_2O_3=11.9-13.8 wt.%, Total FeO=0.99-1.53 wt.%, MgO=0.12-0.33 wt.%, CaO=0.9-1.6 wt.%, NaO_2=3.78-4.88 wt.% and K_2O=2.38-3.37 wt.% (n=239; Table 3; Figa. 8a-d). The darkest material within the mingled pumice is basaltic and ranges down to 48.63 wt.% SiO_2, 7.91 wt.% Al_2O_3, 12.42 wt.% Total FeO, 12.03 wt.% MgO, and 15.02 wt.% CaO (Table 3; Figs. 8a-d). These grey bands are heterogenous in composition and extend from the least evolved composition to SiO_2 concentrations up to 68.5 wt.%. The whole-rock XRF data plot between this dacitic composition and the dominant rhyolite (Figs. 8a-d).

7. Discussion

The volume of material erupted during the TBJ eruption was ~58 km^3 of bulk rock, equivalent to ~30 km^3 DRE of magma and corresponding to a magnitude of 6.8 (Pyle, 2000) (Table 1). Eight units can be identified in the deposits that provide evidence for distinct eruptive styles. The sedimentological and lithological characteristics of these deposits suggest that the TBJ eruption included phases associated with pure magmatic activity and those characterized by magma–water interaction, which are also seen in older intra-caldera deposits (Mann et al., 2004; Suñe-Puchol et al., 2019a,b). Paleosols separate the TBJ from previous eruption deposits at several outcrops (Fig. 2). The repose period before the TBJ was of a sufficient length for this pedogenesis to occur, and the caldera was probably quiescent for around 8 ka, i.e. since TB2 (Kutterolf et al., 2008).

Unit A_0 (less than 0.1 km^3 total DRE volume - Table 1) represents the onset of the TBJ eruption. The field characteristics (Figs. 3a,b) and granulometric analysis (poorly sorted deposit, positive grain-size skewness values-and a bimodal trend; Supplementary material 4b, e, j) suggest that this unit was deposited by dilute PDCs (Branney and Kokelaar, 2002; Dellino et al., 2004a,b; Brand and White, 2007; Brand and Clarke, 2009). The high proportion of mafic lithic fragments is consistent with explosive excavation of the conduit and vent (Fig. 9a), as described in other studies e.g. Vesuvius, Italy (Barberi et al., 1989) and the AD1630 eruption of Furnas volcano, San Miguel, Azores (Cole et al., 1995). These surge clouds had a high momentum as they travelled at least up to 15-20 km from the vent. The deposits show similar field characteristics to the ones of the Layer LM1 from the Lower Member of the Neapolitan Yellow Tuff that represented the onset of the eruption (Orsi et al., 1992). Grain size and componentry (fine-grained deposits; Fig. 4h and high mafic lithic content - Fig. 2), as well as ash deposits suggest that there was magma-water interaction (Self and Sparks, 1978; Barberi et al., 1989; Houghton and Schmincke, 1989; Houghton and Smith, 1993; Cole et al., 1995; Dellino and La Volpe, 1995; De Rita et al., 2002). The opening phases of volcanic eruptions present favourable conditions for magma-water interaction, similar to other case studies such as the Minoan, Santorini Island, Greece, AD79 Vesuvius, Italy (Cioni et al., 2000), Etna 122BC, Italy (Coltelli et al., 1998), and Tarawera AD1886, New Zealand (Houghton et al. 2004) eruptions.

The explosive eruptions that formed Unit A (Fig. 9b) produced an eruptive column that rose to 29 km (Table 1) and it spread mainly westwards in the proximal and medial area. Field evidence (Figs. 3a,b) and granulometric data (well-sorted deposit and a unimodal trend; Supplementary material 4b-f and 4k) of samples are consistent with a tephra fallout deposit (0.15 km^3 total DRE volume - Table 1). Unit A was most likely hydromagmatic, due to the high lithic content (Fig. 2) and fine grain size at medial locations (Supplementary Material 4k) and a distribution mainly to the south of the caldera (Fig. 5a). Passing from dilute PDCs of Unit A_0 to fallout deposits of Unit A is probably related to changes in magma-water mass ratio, which has been observed at several historical hydromagmatic eruptions, e.g. Kilauea volcano, Hawaii, AD1790 (McPhie et al., 1990) or Capelinhos (1957-1958) in Faial, Azores (Cole et al., 2001).

Concerning the first two phases (A_0 and A), the magma-water mass ratio promoted a more or less high explosive efficiency, from wet PDCs and fallout deposits towards drier lapilli fall (Unit B), so the magmatic fragmentation became progressively more dominant. Then, the eruption entered a magmatic fall-dominated phase (Fig. 9c) that formed Unit B (Fig. 3c), which is characterized by highly vesiculated juvenile products released through a ~7-km-high column (Tab. 1) with a grain-supported deposit mainly oriented southwestwards from the source (Fig. 5b). This eruption phase produced a coarse, generally medium sorted (Supplementary Material 4a,b,d,e), pumice fall deposit with a 0.22 km^3 total DRE volume (Table 1). General drier conditions can be related to any factors such as, for example, the variations in magma flux or availability of water in the system, or in some cases, some batches of magma can reach the surface without explosive interaction with water, similarly to maar-diatreme eruptions (Valentine and White, 2012). Similar activity was observed for the C11 deposits of Caldeira Volcano, Faial Island, Azores (Pimentel et al., 2015). The eruption was characterized at the beginning by a series of hydromagmatic eruptions with fallout and PDCs deposits and a subsequent more dominant magmatic fragmentation, due to the rapid draining of magma from the conduit, with the establishment of a sub-Plinian column. The increase in the dispersal area and grain size features in the deposits (Supplementary Material 4g, h, i, l, m, n) indicates steady growth of the eruption column. The column reached its climax without major fluctuations, as there are internal bedding features and the deposits lack normal or inverse grading. This was probably facilitated by the gradual stabilization of the conduit walls associated with increasing vent diameter and magma discharge rate.

Unit C (0.5 km^3 total DRE volume - Table 1) represents an abrupt change in the eruption dynamics (Fig. 9d). This well-sorted (Supplementary Material 4a-c), massive, lithic-poor and ash-rich deposit (Supplementary Material 4d-f and g-i), with few dispersed pumice fragments and accretionary lapilli indicate deposition from PDCs (Fig. 3a) that flowed mainly to the south-east part of the IC (Fig. 5c). These dynamics were probably due to the shift of the vent location and a subsequent interaction of magma with external water that led to an enhanced magma fragmentation, as well as a greater explosivity of the eruption that contributed to the generation of fine ash (Supplementary Material 4o-q). The stratigraphic position of these hydromagmatic deposits immediately above the magmatic deposits suggests a subsequent access of the lake water to the column of rising magma. However, we cannot discount the role of hydrothermal and groundwater in the hydromagmatic episode that lead to the emplacement of Unit C. The presence of hydrothermally altered lithic fragments suggests the occurrence of an extensive hydrothermal system within the caldera at the time of the eruption (Saxby et al., 2016).

Unit D (3.3 km^3 total DRE volume - Table 1) shows similar field characteristics (Fig. 3d,e) and granulometric data (Supplementary Material 4 a-c and r-t) to the previous unit C (Fig. 3d), and suggest it was emplaced from PDCs of hydromagmatic origin (Fig. 9d). The hydrothermally altered lithic fragments observed in Unit C are not recognized in the Unit D, so the ongoing magma-water interaction was most likely fuelled by surface water. There was probably a shallow lake in the IC at ≥43.670 ka years ago as proposed by Mann et al. (2004). As suggested by Aravena et al. (2018), natural aquifers appear unlikely to be sources of enough water to significantly affect the eruptive dynamics of an event with high mass discharge rate; conversely, evidence for magma-water interaction are probably related to the involvement of surface water or the injection of groundwater by high-magnitude collapse mechanisms. The same type of activity was also reported for Taal caldera lake, Philippines in 1991 (Delmelle and Bernard, 2000), the hydromagmatic eruption of Kilauea Volcano, Hawaii, in 1970 (Mastin, 1997), or the Nari Caldera at Ulleung Island, Korea (Kim et al., 2014). Changes from dry to wet conditions in such eruptions were also observed for the Askja 1875 eruption, Iceland (Sparks et al., 1981; Carey et al., 2010) and the AD232 Taupo eruption, New Zealand (Houghton et al., 2000). The absence of any fall deposits at the base of Units C and D rules out the possibility of a sustained eruptive column phase (Fig. 5d).

During the course of the eruption, there was another change in the eruptive dynamics, with a switch to drier conditions (Fig. 9e). Unit E (0.3 km^3 total DRE volume - Table 1) was deposited by alternation of dilute PDCs and fallout, which is based on plane-parallel and low-angle cross laminations and grain-supported layers without traction structures (Fig. 3f; Chough and Sohn, 1990; De Rosa et al., 1992; Dellino et al., 2004b; Solgevik et al., 2007), alternation of well and poorly sorted deposits (Supplementary Material4 a-c) of ash and lapilli (Supplementary Material4 g-i), and a clear polymodal trend of the grain size distribution (Supplementary Material 4 u-w). Soft sediment folding (Fig. 3g) might indicate that some of the layers were deposited wet as consequence of magma-water interaction, thus characterizing the whole unit as alternation of dry and wet deposits that were deposited around the IC (Fig. 5e). At this time, due to structural faults that characterize IC, the magma might have had interaction with the almost empty Ilopango Lake after Unit D phase, thus allowing an intermittent magma-water interaction with the formation of short-lived columns and lateral blast.

It is important to consider how, not only a change in the water-magma ratio might have led to the emplacement of fallout and PDCs deposits, but also the scaled depth (ratio between depth of explosion and energy) can have huge effects on deposit characteristics, grain size and deposit morphology (see Taddeucci et al. 2013; Graettinger et al. 2014, 2015; Valentine et al. 2014, 2015; Sonder et al. 2015). As suggested in Graettinger et al. (2015), when scaled depth is constant, the crater focuses the jet and results in decreasing overall volumes of coarse ejecta and the potential occurrence of fine-grained dilute density current deposits. Progressively increasing scaled depth results in an overall decrease in ejecta volume to the point where the explosion is confined and no ejecta are produced. A progressive decrease in scaled depth will result in an increase in ejecta volume and in the grain size of ejecta deposits and low occurrence of fine-grained dilute density currents as the jet is larger than the previous crater and therefore does not exhibit significant focusing.

The final phase (Fig. 9f) of the eruption was marked by a dramatic change in eruptive style with deposition of chaotic, massive, poorly-sorted (Supplementary Material4a-c), non-welded dry thick PDC deposits (Figs. 3h, i). The lag-breccia deposits of Unit F are observed only close to the caldera topographic edge (Figs. 3j). This might be related to the strong control exerted by the paleotopography on facies architecture as observed, for example, for the Abrigo Ignimbrite in Tenerife, Canary Islands (Pittari et al., 2006) or the Acatlán ignimbrite, Mexico (Branney and Kokelaar, 1997). This is a lithic-rich ignimbrite that represents continued clearing from fissure vents along the main bounding caldera faults (Fig. 9f). The sharp, erosive lower contact with underlying units, coarse, up to meter-sized lithic clasts and juveniles in a poorly sorted matrix (Figs. 3h-k), together with granulometric analyses (Supplementary Material 4g-i and x-z), suggest eruptive dynamics that were dominated by vigorous and prolonged pyroclastic fountaining that produced sustained quasi-steady PDCs, as the eruption waxed and stabilized. Both basal high-particle concentrations in the PDCs and the long runout distances were maintained because of the continuous supply of dense currents at the vent (Roche et al., 2016). These deposits formed an ignimbrite sheet, Unit F (9.3 km^3 total DRE volume-Tab. 1) that reached the sea on southern sectors of the caldera and was widespread around IC (Fig. 5f). At this point, the increase in the magma eruption rate could have been produced by the start of the caldera collapse, which would have commenced the rapid evacuation of magma from the sub-caldera magma chamber, leading to a subsequent inefficient magma-water interaction during F eruptive phase. Similar mechanisms from wet to drier conditions were also observed during the Neapolitan Yellow Tuff eruption (Orsi et al., 1992). The mingled pumice clasts that extend to basaltic compositions are also found in deposits from this phase of the eruption suggesting that additional melts were erupted. Since these distinctive less evolved compositions are restricted to the clasts in the very proximal outcrops it implies that the erupted volume of this melt was incredibly small. It is quite common for additional melts to be erupted during caldera formation (cf. Smith et al., 2016).

As for Units C and D, no fallout layers were recognized at the base of Unit F, thus, suggesting that an initial buoyant Plinian eruption column-building phase was not produced. This feature is similar to other ignimbrites such as Campanian (Marti et al., 2016) and Ora in Italy (Willcock et al., 2013), or Huichapan in Mexico (Pacheco et al., 2018). The occurrence of fines-poor elutriation pipes (Fig. 3l) indicates that following deposition, vigorous gas escape occurred elutriating fines. These pipes are interpreted as evidence of rapid emplacement involving particle segregation and vigorous, post emplacement fluid (dusty gas) escape (Branney and Kokelaar, 2002), thus suggesting that at the time of deposition Unit F deposits were hot.

Unit G (Fig. 3n) represents the final co-ignimbritic deposit of the TBJ eruption (Fig. 9g). Deposits were found at medial and distal locations that are more than 100 km from the caldera (Fig. 3o). This unit is made of moderately to poorly sorted (Supplementary Material 4a-c) ash (Supplementary Material 4 g-i) with a clear bimodality grain-size distribution trend (Supplementary Material 4aa-ac) that highlights the significance of ash aggregation processes in the transport and deposition.

The absence of Plinian pumice fall deposits preceding the dense PDC deposits of TBJ is a typical characteristic of graben-type calderas as Ilopango (Aguirre-Díaz and Martí, 2015; Aguirre-Díaz et al., 2016, 2017; Saxby et al., 2016; Sunye-Puchol et al., 2019a) or fissure ignimbrite eruptions related to local/regional faults (Aguirre-Díaz and Labarthe-Hernández, 2003; Aguirre-Díaz et al., 2008). This is due to the significant control of tectonic stress on mass discharge rate (Costa et al., 2011; Costa and Martí, 2016), with graben-type calderas tending to generate large MER larger that are too high to sustain a Plinian column (see Costa et al, 2018).

The TBJ deposits highlight that a single eruption can produce a complex sequence of eruption styles and depositional processes. The magnitude of this eruption means that Mayan populations living in the region would have been considerably affected (Dull et al., 2001; Hernández, 2004; Hernández et al., 2015). The human populations directly affected by the TBJ eruption would have been those living in the territory within 50 km of the IC. However, the indirect effects on social, economic, and political systems probably affected a much wider area of Mesoamerica (Dull et al., 2001). It has also been suggested that the sulphate peak, typically associated with volcanic eruptions, in the both Greenland and Antarctic ice cores at AD 539-540 could be associated with the TBJ eruption (Sigl et al., 2015). These peaks are associated with the H_2SO_4 aerosols that are injected into the high atmosphere during large volcanic eruptions, which increase the albedo and potentially produce a volcanic winter period (Robock, 2000). However, the date of the eruption has not been sufficiently resolved to establish if these sulphate peaks in the polar ice cores are in fact associated wit the TBJ eruption as the ^{14}C dates fall on a plateau in the radiocarbon calibration curve (e.g., Reimer et al., 2013), which results in an imprecise eruption range of AD270-AD400 (Lohse et al., 2018) to AD440-550 (Dull et al. 2010).

The examination of this eruption sheds light on a number of important implications for hazard assessment when considered within the framework of the volcanism associated with IC and Country of El Salvador. The detailed study of the TBJ eruption together with the one of Suné-Puchol et al. (2019a,b) about the older eruptions of IC, represent the first and necessary step towards improved volcanic hazard assessments for the region. These are essential to mitigate volcanic risk for the large number of communities, including the City of San Salvador, that are expanding around this active volcano.

Conclusion

In this study, we conducted a detailed stratigraphic and lithological study of the dacitic pumice Tierra Blanca Joven (TBJ) deposit. The TBJ is the last explosive eruption of Ilopango Caldera, representing a singular eruptive episode and constitutes the last eruptive cycle of the Tierra Blanca sequence that starts with the TB4 eruption deposit. The TBJ eruption erupted ~58 km^3 of bulk volume rock or ~30 km^3 DRE of magma, corresponding to a 6.8 magnitude eruption.

The eruption was characterized by eight phases (A_0-G) with distinct eruptive styles without major pauses in between. The eruption started with dilute PDCs followed by two fallout phases that left only few cm of deposits, found mainly close to the IC. Subsequently, dense and dilute PDCs of hydromagmatic and magmatic origin filled the depressions near the Ilopango Lake. Deposits thicknesses are up to 70 m and reached distances of at least 40 km from the vent, covering the area where the city of San Salvador is now located. Finally, coignimbritic ash deposits of the last stage of the eruption were found all over El Salvador with significant thicknesses, and also found dispersed into neighbouring countries.

The TBJ was a cataclysmic event and is considered to be one of the largest Quaternary eruptions in Central America. TBJ eruptive products would have considerably affected the Mayan populations living in Salvadorian and nearby territories at that time. Consequently, long- and short-term hazard assessments for IC should take into account all possible scenarios including those described for the TBJ eruption.

Acknowledgements

This study was financed by CONACYT-CB grant 240447 and logistically supported by MARN-El Salvador and PNC-El Salvador. We thank Caterina Muñoz Torres, Academic Technician of CGEO and the students Karina Rodríguez García and Katia Jasso Torres for their help during the survey. This manuscript was greatly improved by comments and suggestions from the chief-editor Joan Martí and an anonymous reviewer.

References

Aguirre-Díaz, G.J., 2008. Types of collapse calderas. Collapse Calderas Workshop 19–25 October 2008, Querétaro, Mexico "Reconstructing the Evolution of Collapse Calderas: Magma Storage, Mobilization and Eruption". IOP Conference Series: Earth and Environmental Science, 3 012021 (5pp).

Aguirre-Díaz, G.J. and Labarthe-Hernández, G., 2003. Fissure ignimbrites: Fissure-source origin for voluminous ignimbrites of the Sierra Madre Occidental and its relationship with Basin and Range faulting. Geology, 31(9): 773-776.

Aguirre-Díaz, G.J., Labarthe-Hernández, G., Tristán-González, M., Nieto-Obregón, J. and Gutiérrez-Palomares, I., 2008. The ignimbrite flare-up and graben calderas of the Sierra Madre Occidental, Mexico. Developments in Volcanology, 10: 143-180.

Aguirre-Díaz, G.J. and Martí, J., 2015. Graben calderas: Examples from Mexico, Central America, and the Andes. 26th IUGG General Assembly, Prague, Czech Republic, June 22-July 2, 2015.

Aguirre-Díaz, G.J., Suñe-Puchol, I., Dávila-Harris, P., Pedrazzi, D., Hernández, W. and Gutiérrez, E., 2016. Volcanic history of the Ilopango caldera, Central American Volcanic Arc:. Cities on Volcanoes 9, IAVCEI; Puerto Varas, Chile, November 2016.

Aguirre-Díaz, J.G., Suñe-Puchol, I., Davila-Harris, P., Pedrazzi, D., Hernandez, W. and Gutierrez, E., 2017 Volcanic history of the Ilopango caldera, Central American Volcanic Arc. . 113th Annual Meeting, 2017 GSA Cordilleran Section, Hawaii, USA.

Aravena, A., Vitturi, M., Cioni, R. and Neri, A., 2018. Physical constraints for effective magma-water interaction along volcanic conduits during silicic explosive eruptions. Geology, 46(10): 867-870.

Barberi, F., Cioni, R., Rosi, M., Santacroce, R., Sbrana, A. and Vecci, R., 1989. Magmatic and phreatomagmatic phases in explosive eruptions of Vesuvius as deduced by grain-size and component analysis of the pyroclastic deposits. Journal of Volcanology and Geothermal Research, 38(3): 287-307.

Barckhausen, U., Ranero Cesar, R., Huene, R., Cande Steven, C. and Roeser Hans, A., 2001. Revised tectonic boundaries in the Cocos Plate off Costa Rica: Implications for the segmentation of the convergent margin and for plate tectonic models. Journal of Geophysical Research: Solid Earth, 106(B9): 19207-19220.

Bernal, J.B. and Lozano-Santacruz, R., 2005. Characterization of a new set of eight geochemical reference materials for XRF major and trace element analysis. Revista Mexicana de Ciencias Geológicas, 22(3): 329-344.

Bonadonna, C. and Costa, A., 2012. Estimating the volume of tephra deposits: A new simple strategy. Geology, 40(5): 415-418.

Bonadonna, C. and Costa, A., 2013. Plume height, volume, and classification of explosive volcanic eruptions based on the Weibull function. Bulletin of Volcanology, 75(8): 742.

Bonadonna, C. and Houghton, B.F., 2005. Total grain-size distribution and volume of tephra-fall deposits. Bulletin of Volcanology, 67(5): 441-456.

Brand, B.D. and Clarke, A.B., 2009. The architecture, eruptive history, and evolution of the Table Rock Complex, Oregon: From a Surtseyan to an energetic maar eruption. Journal of Volcanology and Geothermal Research, 180(2): 203-224.

Brand, B.D. and White, C.M., 2007. Origin and stratigraphy of phreatomagmatic deposits at the Pleistocene Sinker Butte Volcano, Western Snake River Plain, Idaho. Journal of Volcanology and Geothermal Research, 160(3): 319-339.

Branney, M.J. and Kokelaar, P., 1997. Giant bed from a sustained catastrophic density current flowing over topography: Acatlan ignimbrite, Mexico. Geology, 25(2): 115-118.

Branney, M.J. and Kokelaar, P., 2002. Pyroclastic density currents and the sedimentation of ignimbrites. Geological Society of London.

Canora, C., Villamor, P., Martínez-Díaz, J.J., Berryman, K.R., Álvarez-Gómez, J.A., Capote, R. and Hernández, W., 2012. Paleoseismic analysis of the San Vicente segment of the El Salvador Fault Zone, EL Salvador, Central America. . Geologica Acta, 10: 103-123.

Carey, R.J., Houghton, B.F. and Thordarson, T., 2010. Tephra dispersal and eruption dynamics of wet and dry phases of the 1875 eruption of Askja Volcano, Iceland. Bulletin of Volcanology, 72(3): 259-278.

Carr, M.J., Patino, L.C. and Feigenson, M.D., 2007. Petrology and geochemistry of lavas. Central America: geology, resources and hazards. 1 565-577.

Chough, S.K. and Sohn, Y.K., 1990. Depositional mechanics and sequences of base surges, Songaksan tuff ring, Cheju Island, Korea. Sedimentology, 37(6): 1115-1135.

Cioni, R., Gurioli, L., Sbrana, A. and Vougioukalakis, G., 2000. Precursory phenomena and destructive events related to the Late Bronze Age Minoan (Thera, Greece) and AD 79 (Vesuvius, Italy) Plinian eruptions; inferences from the stratigraphy in the archaeological areas. Geological Society, London, Special Publications, 171(1): 123-141.

Cole, P.D., Guest, J.E., Duncan, A.M. and Pacheco, J.-M., 2001. Capelinhos 1957–1958, Faial, Azores: deposits formed by an emergent surtseyan eruption. Bulletin of volcanology, 63(2-3): 204.

Cole, P.D., Queiroz, G., Wallenstein, N., Gaspar, J.L., Duncan, A.M. and Guest, J.E., 1995. An historic subplinian/phreatomagmatic eruption: the 1630 AD eruption of Furnas volcano, São Miguel, Azores. Journal of volcanology and geothermal research, 69(1-2): 117-135.

Coltelli, M., Del Carlo, P. and Vezzoli, L., 1998. Discovery of a Plinian basaltic eruption of Roman age at Etna volcano, Italy. Geology, 26(12): 1095-1098.

Corti, G., Carminati, E., Mazzarini, F. and Garcia, M.O., 2005. Active strike-slip faulting in El Salvador, Central America. Geology, 33(12): 989-992.

Costa, A., Dell'Erba, F., Di Vito, M.A., Isaia, R., Macedonio, G., Orsi, G. and Pfeiffer, T., 2009. Tephra fallout hazard assessment at the Campi Flegrei caldera (Italy). Bulletin of Volcanology, 71(3): 259.

Costa, A., Gottsmann, J., Melnik, O. and Sparks, R.S.J., 2011. A stress-controlled mechanism for the intensity of very large magnitude explosive eruptions. Earth and Planetary Science Letters, 310(1-2): 161-166.

Costa, A. and Martí, J., 2016. Stress Field Control during Large Caldera-Forming Eruptions. Frontiers in Earth Science, 4(92).

Costa, A., Suzuki, J.Y. and Koyaguchi, T., 2018. Understanding the plume dynamics of explosive super-eruptions. Nature Communications, 9(1): 654.

Daugherty, H.E., 1969 Man-Induced Ecological Change in El Salvador. Ph.D. dissertation, University of California, Los Angeles. University Microfilms, Ann Arbor.

De Rita, D., Giordano, G., Esposito, A., Fabbri, M. and Rodani, S., 2002. Large volume phreatomagmatic ignimbrites from the Colli Albani volcano (Middle Pleistocene, Italy). Journal of Volcanology and Geothermal Research, 118(1-2): 77-98.

De Rosa, R., Frazzetta, G. and La Volpe, L., 1992. An approach for investigating the depositional mechanism of fine-grained surge deposits. The example of the dry surge deposits at "La Fossa di Vulcano". Journal of Volcanology and Geothermal Research, 51(4): 305-321.

Dellino, P., Isaia, R., La Volpe, L. and Orsi, G., 2004a. Interaction between particles transported by fallout and surge in the deposits of the Agnano–Monte Spina eruption (Campi Flegrei, Southern Italy). Journal of Volcanology and Geothermal Research, 133(1): 193-210.

Dellino, P., Isaia, R. and Veneruso, M., 2004b. Turbulent boundary layer shear flows as an approximation of base surges at Campi Flegrei (Southern Italy). Journal of Volcanology and Geothermal Research, 133(1): 211-228.

Dellino, P. and La Volpe, L., 1995. Fragmentation versus transportation mechanisms in the pyroclastic sequence of Monte Pilato-Rocche Rosse (Lipari, Italy). Journal of Volcanology and Geothermal Research, 64(3-4): 211-231.

Delmelle, P. and Bernard, A., 2000. Downstream composition changes of acidic volcanic waters discharged into the Banyupahit stream, Ijen caldera, Indonesia. Journal of Volcanology and Geothermal Research, 97(1): 55-75.

DeMets, C., 2001. A new estimate for present-day Cocos-Caribbean Plate motion: Implications for slip along the Central American Volcanic Arc. Geophysical Research Letters, 28(21): 4043-4046.

DeMets, C., Jansma, P.E., Mattioli, G.S., Dixon, T.H., Farina, F., Bilham, R., Calais, E. and Mann, P., 2000. GPS geodetic constraints on Caribbean-North America Plate Motion. Geophysical Research Letters, 27(3): 437-440.

Denevan, W.M., 1992 Introduction. In The Native Population of the Americas in 1492. 2nd ed. Edited by William M. Denevan, pp. xv-xli. University of Wisconsin Press, Madison.

Dixon, T.H., 1993. GPS measurement of relative motion of the Cocos and Caribbean Plates and strain accumulation across the Middle America Trench. Geophysical Research Letters, 20(20): 2167-2170.

Dull, R., Southon, J., Kutterolf, S., Freundt, A., Wahl, D. and Sheets, P., 2010. Did the Ilopango TBJ eruption cause the AD 536 event, AGU Fall meeting, Abstracts.

Dull, R.A., Southon, J.R. and Sheets, P., 2001. Volcanism, ecology and culture: A reassessment of the Volcán Ilopango TBJ eruption in the southern Maya realm. Latin American Antiquity, 12(1): 25-44.

Funk, J. and Mann, P., 2009. Cenozoic tectonics of the Nicaraguan depression, Nicaragua, and Median Trough, El Salvador, based on seismic-reflection profiling and remote-sensing dataCenozoic tectonics of the Nicaraguan depression. GSA Bulletin, 121(11-12): 1491-1521.

Garibaldi, N., Tikoff, B. and Hernández, W., 2016. Neotectonic deformation within an extensional stepover in El Salvador magmatic arc, Central America: Implication for the interaction of arc magmatism and deformation. Tectonophysics, 693: 327-339.

Golombek, M.P. and Carr, M.J., 1978. Tidal triggering of seismic and volcanic phenomena during the 1879–1880 eruption of Islas Quemadas volcano in El Salvador, Central America. Journal of Volcanology and Geothermal Research, 3(3-4): 299-307.

Graettinger, A.H., Valentine, G.A., Sonder, I., Ross, P.-S. and White, J.L., 2015. Facies distribution of ejecta in analog tephra rings from experiments with single and multiple subsurface explosions. Bulletin of Volcanology, 77(8): 66.

Graettinger, A.H., Valentine, G.A., Sonder, I., Ross, P.S., White, J.D.L. and Taddeucci, J., 2014. Maar‐diatreme geometry and deposits: Subsurface blast experiments with variable explosion depth. Geochemistry, Geophysics, Geosystems, 15(3): 740-764.

Guzmán-Speziale, M., Valdés-González, C., Molina, E. and Gómez, J.M., 2005. Seismic activity along the Central America volcanic arc: Is it related to subduction of the Cocos plate? Tectonophysics, 400(1-4): 241-254.

Hart, W.J.E., 1981. The Panchimalco tephra, El Salvador, Central America. M.S. thesis: New Brunswick, New Jersey, Rutgers University: 101 p.

Hart, W.J.E. and Steen-McIntyre, V., 1983. Tierra Blanca Joven Tephra from the AD 260 eruption of Ilopango caldera. Archeology and Volcanism in Central America—The Zapotitán Valley of El Salvador: 15-34.

Hernández, E.W., 2004 Características geotécnicas y vulcanológicas de las tefras de Tierra Blanca Joven de Ilopango, El Salvador. Tesis de maestría, Univ. Politécnica de El Salvador, San Salvador: 115 p.

Hernández, E.W., Ferrés, D., Delgado-Granados, H., Pullinger, C. and Gutiérrez de Henríquez, E., 2010. The last 40 ka eruptive cycle of Ilopango caldera deposits: a settlement for the San Salvador Metropolitan Area (El Salvador). A. Abstract volume, International Conference Cities on Volcanoes, Fundación Canaria ITER, Tenerife: pp 56.

Hernández, W., Aguirre-Díaz, G. and Ayala, P., 2015. La erupción Tierra Blanca Joven y la diáspora de los Mayas. Museo Nacional de Antropología David J. Guzmán, V Congreso Centroamericano de Arqueología en El Salvador. José Erquicia y Shione Shibata editores. 238p. ISBN 978-99961-958-0-8: 227-237.

Hernández, W., Delgado-Granados, H. and Nieto, J., 2012. La erupción Tierra Blanca 4 (TB4), Caldera de Ilopango, El Salvador. . Ministerio de Medio Ambiente y Recursos Naturales, Informe inédito: 36 p.

Houghton, B.F. and Schmincke, H.-U., 1989. Rothenberg scoria cone, East Eifel: a complex Strombolian and phreatomagmatic volcano. Bulletin of Volcanology, 52(1): 28-48.

Houghton, B.F. and Smith, R.T., 1993. Recycling of magmatic clasts during explosive eruptions: estimating the true juvenile content of phreatomagmatic volcanic deposits. Bulletin of Volcanology, 55(6): 414-420.

Houghton, B.F., Smith, R.T. and Gilbert, J.S., 2000. Phreatoplinian eruptions. Encyclopedia of volcanoes: 513-525.

Houghton, B.F., Wilson, C.J.N., Del Carlo, P., Coltelli, M., Sable, J.E. and Carey, R.J., 2004. The influence of conduit processes on changes in style of basaltic Plinian eruptions: Tarawera 1886 and Etna 122 BC. Journal of Volcanology and Geothermal Research, 137(1-3): 1-14.

Hutton, D.H.W. and Reavy, R.J., 1992. Strike‐slip tectonics and granite petrogenesis. Tectonics, 11(5): 960-967.

Jochum Klaus, P., Stoll, B., Herwig, K., Willbold, M., Hofmann, A.W., Amini, M., Aarburg, S., Abouchami, W., Hellebrand, E., Mocek, B., Raczek, I., Stracke, A., Alard, O., Bouman, C., Becker, S., Dücking, M., Brätz, H., Klemd, R., de Bruin, D., Canil, D., Cornell, D., de Hoog, C.J., Dalpé, C., Danyushevsky, L., Eisenhauer, A., Gao, Y., Snow, J.E., Groschopf, N., Günther, D., Latkoczy, C., Guillong, M., Hauri, E.H., Höfer, H.E., Lahaye, Y., Horz, K., Jacob, D.E., Kasemann, S.A., Kent, A.J.R., Ludwig, T., Zack, T., Mason, P.R.D., Meixner, A., Rosner, M., Misawa, K., Nash, B.P., Pfänder, J., Premo, W.R., Sun, W.D., Tiepolo, M., Vannucci, R., Vennemann, T., Wayne, D. and Woodhead, J.D., 2006. MPI-DING reference glasses for in situ microanalysis: New reference values for element concentrations and isotope ratios. Geochemistry, Geophysics, Geosystems, 7(2).

Kutterolf, S., Freundt, A. and Perez, W., 2008b. Pacific offshore record of plinian arc volcanism in Central America: 2. Tephra volumes and erupted masses. Geochemistry, Geophysics, Geosystems, 9(2).

Kutterolf, S., Freundt, A., Perez, W., Mörz, T., Schacht, U., Wehrmann, H. and Schmincke, H.U., 2008a. Pacific offshore record of plinian arc volcanism in Central America: 1. Along-arc correlations. Geochemistry, Geophysics, Geosystems, 9(2).

LaFemina, P., Dixon Timothy, H., Govers, R., Norabuena, E., Turner, H., Saballos, A., Mattioli, G., Protti, M. and Strauch, W., 2009. Fore-arc motion and Cocos Ridge collision in Central America. Geochemistry, Geophysics, Geosystems, 10(5).

Le Bas, M.J., Le Maitre, R.W., Streckeisen, A., Zanettin, B. and Rocks, I.S.o.t.S.o.I., 1986. A chemical classification of volcanic rocks based on the total alkali-silica diagram. Journal of petrology, 27(3): 745-750.

Leake, B.E., Woolley, A.R., Arps, C.E., Birch, W.D., Gilbert, M.C., Grice, J.D., Hawthorne, F.C., Kato, A., Kisch, H.J. and Krivovichev, V.G., 1997. Report. Nomenclature of amphiboles: report of the subcommittee on amphiboles of the international mineralogical association commission on new minerals and mineral names. Mineralogical magazine, 61(2): 295-321.

Lexa, J., Sebesta, J., Chávez, J.A., Hernández, W. and Pecskay, Z., 2011. Geology and volcanic evolution in the southern part of the San Salvador Metropolitan Area. Journal of Geosciences, 56(1): 106-140.

Lohse, J.C., Hamilton, W.D., Brenner, M., Curtis, J., Inomata, T., Morgan, M., Cardona, K., Aoyama, K. and Yonenobu, H., 2018. Late Holocene volcanic activity and environmental change in Highland Guatemala. Quaternary Science Reviews, 191: 378-392.

Lovell, W.G. and Lutz, C.H., 1995 Demography and Empire. Dellplain Latin American Studies, Number 33. Westview Press, Boulder.

Macedonio, G., Costa, A. and Longo, A., 2005. A computer model for volcanic ash fallout and assessment of subsequent hazard. Computers & Geosciences, 31(7): 837-845.

Macedonio, G. and Pareschi, M.T., 1991. An algorithm for the triangulation of arbitrarily distributed points: applications to volume estimate and terrain fitting. Computers & Geosciences, 17(7): 859-874.

Mann, C.P., Stix, J., Vallance, J.W. and Richer, M., 2004. Subaqueous intracaldera volcanism, Ilopango Caldera, El Salvador, Central America, . in Rose, W.I., Bommer, J.J., López, D.L., Carr, M.J., and Major, J.J., eds., Natural hazards in El Salvador: Boulder, Colorado, Geological Society of America Special Paper 375: 159–174.

Mann, P., 2007. Overview of the tectonic history of northern Central America. Geological Society of America Special Papers, 428: 1-19.

Marti, A., Folch, A., Costa, A. and Engwell, S., 2016. Reconstructing the plinian and co-ignimbrite sources of large volcanic eruptions: A novel approach for the Campanian Ignimbrite. Scientific reports, 6: 21220.

Martí, J., Groppelli, G. and Brum da Silveira, A., 2018. Volcanic stratigraphy: A review. Journal of Volcanology and Geothermal Research, 357: 68-91.

Martínez-Díaz, J.J., Álvarez-Gómez, J.A., Benito, B. and Hernández, D., 2004. Triggering of destructive earthquakes in El Salvador. Geology, 32(1): 65-68.

Mastin, L.G., 1997. Evidence for water influx from a caldera lake during the explosive hydromagmatic eruption of 1790, Kilauea volcano, Hawaii. Journal of Geophysical Research: Solid Earth, 102(B9): 20093-20109.

Mastin, L.G., Guffanti, M., Servranckx, R., Webley, P., Barsotti, S., Dean, K., Durant, A., Ewert, J.W., Neri, A., Rose, W.I., Schneider, D., Siebert, L., Stunder, B., Swanson, G., Tupper, A., Volentik, A. and Waythomas, C.F., 2009. A multidisciplinary effort to assign realistic source parameters to models of volcanic ash-cloud transport and dispersion during eruptions. Journal of Volcanology and Geothermal Research, 186(1): 10-21.

Matthews, N.E., Smith, V.C., Costa, A., Durant, A.J., Pyle, D.M. and Pearce, N.J.G., 2012. Ultra-distal tephra deposits from super-eruptions: Examples from Toba, Indonesia and Taupo Volcanic Zone, New Zealand. Quaternary International, 258: 54-79.

McPhie, J., Walker, G.P.L. and Christiansen, R.L., 1990. Phreatomagmatic and phreatic fall and surge deposits from explosions at Kilauea volcano, Hawaii, 1790 AD: Keanakakoi Ash Member. Bulletin of Volcanology, 52(5): 334-354.

Montero, W. and Dewey, J., 1982. Shallow-focus seismicity, composite focal mechanism, and tectonics of the Valle Central of Costa Rica. Bulletin of the Seismological Society of America, 72(5): 1611-1626.

Morimoto, N., 1989. Nomenclature of pyroxenes. Mineralogical Journal, 14(5): 198-221.

Orsi, G., D'Antonio, M., Vita, S.d. and Gallo, G., 1992. The Neapolitan Yellow Tuff, a large-magnitude trachytic phreatoplinian eruption: eruptive dynamics, magma withdrawal and caldera collapse. Journal of Volcanology and Geothermal Research, 53(1): 275-287.

Pacheco-Hoyos, J.G., Aguirre-Díaz, G.J. and Dávila-Harris, P., 2018. Boiling-over dense pyroclastic density currents during the formation of the ~100km3 Huichapan ignimbrite in Central Mexico: Stratigraphic and lithofacies analysis. Journal of Volcanology and Geothermal Research, 349: 268-282.

Pfeiffer, T., Costa, A. and Macedonio, G., 2005. A model for the numerical simulation of tephra fall deposits. Journal of Volcanology and Geothermal Research, 140(4): 273-294.

Pimentel, A., Pacheco, J. and Self, S., 2015. The~ 1000-years BP explosive eruption of Caldeira Volcano (Faial, Azores): the first stage of incremental caldera formation. Bulletin of Volcanology, 77(5): 42.

Pittari, A., Cas, R.A.F., Edgar, C.J., Nichols, H.J., Wolff, J.A. and Marti, J., 2006. The influence of palaeotopography on facies architecture and pyroclastic flow processes of a lithic-rich ignimbrite in a high gradient setting: the Abrigo Ignimbrite, Tenerife, Canary Islands. Journal of Volcanology and Geothermal Research, 152(3-4): 273-315.

Protti, M., Guendel, F. and McNally, K., 1995. Correlation between the age of the subducting Cocos plate and the geometry of the Wadati-Benioff zone under

Nicaragua and Costa Rica. Special Papers Geological Society of America: 309-309.

Pyle, D.M., 2000. Sizes of volcanic eruptions. In the Encyclopaedia of Volcanoes, (Sigurdsson, H.; Houghton, B.; McNutt, SR; Rymer, H.; Stix, J., editors). Academic Press, London.

Quane, S.L. and Russell, J.K., 2005. Ranking welding intensity in pyroclastic deposits. Bulletin of Volcanology, 67(2): 129-143.

Reimer, P.J., Bard, E., Bayliss, A., Beck, J.W., Blackwell, P.G., Ramsey, C.B., Buck, C.E., Cheng, H., Edwards, R.L. and Friedrich, M., 2013. IntCal13 and Marine13 radiocarbon age calibration curves 0–50,000 years cal BP. Radiocarbon, 55(4): 1869-1887.

Richer, M., Mann, C.P. and Stix, J., 2004. Mafic magma injection triggers eruption at Ilopango Caldera, El Salvador, Central America. Spec. Pap. 375 Nat. Hazards El Salvador 175–190.

Robock, A., 2000. Volcanic eruptions and climate. Reviews of geophysics, 38(2): 191-219.

Roche, O., Buesch, D.C. and Valentine, G.A., 2016. Slow-moving and far-travelled dense pyroclastic flows during the Peach Spring super-eruption. Nature communications, 7: 10890.

Rolo, R., Bommer, J.J., Houghton, B.F., Vallance, J.W., Berdousis, P., Mavrommati, C. and Murphy, W., 2004. Geologic and engineering characterization of Tierra Blanca pyroclastic ash deposits. Special Papers Geological Society of America: 55-68.

Rose, W.I., Conway, F.M., Pullinger, C.R., Deino, A. and McIntosh, W.C., 1999. An improved age framework for late Quaternary silicic eruptions in northern Central America. Bulletin of Volcanology, 61(1): 106-120.

Saxby, J., Gottsmann, J., Cashman, K. and Gutiérrez, E., 2016. Magma storage in a strike-slip caldera. Nature Communications, 7: 12295.

Šebesta, J., 2007. Geomorfología del AMSS y su relación con los movimientos de ladera. Open file report, Czech Geological Survey Prague Oficina de Planificación del Área Metropolitana de San Salvador (OPAMSS): pp 1-40.

Self, S. and Sparks, R.S.J., 1978. Characteristics of widespread pyroclastic deposits formed by the interaction of silicic magma and water. Bulletin Volcanologique, 41(3): 196.

Siebert, L. and Simkin, T., 2002. Volcanoes of the World: an Illustrated Catalogue of Holocene Volcanoes and their Eruptions. Smithsonian Institution, Global Volcanism Program Digital Information Series, GVP-3. (http://www.volcano.si.edu/world/)□.

Sigl, M., Winstrup, M., McConnell, J.R., Welten, K.C., Plunkett, G., Ludlow, F., Büntgen, U., Caffee, M., Chellman, N. and Dahl-Jensen, D., 2015. Timing and climate forcing of volcanic eruptions for the past 2,500 years. Nature, 523(7562): 543.

Simkin, T. and Siebert, L., 1994 Volcanoes of the World2nd Ed. Geoscience Press, Tucson.

Smith, J.V. and Brown, W.L., 1988. Spectroscopy—IR, Raman, NMR, NQR, EPR, NGR (Mössbauer), XAS, EXAFS, ESCA, XPS, Feldspar Minerals. Springer, pp. 244-267.

Smith, V.C., Isaia, R., Engwell, S.L. and Albert, P.G., 2016. Tephra dispersal during the Campanian Ignimbrite (Italy) eruption: implications for ultra-distal ash transport during the large caldera-forming eruption. Bulletin of Volcanology, 78(6): 45.

Sofield, D., 2004. Eruptive history and volcanic hazards of Volcan San Salvador. Geol. Soc. Am. Spec. Pap., 375: 147–158.

Sohn, Y.K. and Chough, S.K., 1989. Depositional processes of the Suwolbong tuff ring, Cheju Island (Korea). Sedimentology, 36(5): 837-855.

Solgevik, H., Mattsson, H.B. and Hermelin, O., 2007. Growth of an emergent tuff cone: Fragmentation and depositional processes recorded in the Capelas tuff cone, São Miguel, Azores. Journal of Volcanology and Geothermal Research, 159(1): 246-266.

Sonder, I., Graettinger, A.H. and Valentine, G.A., 2015. Scaling multiblast craters: General approach and application to volcanic craters. Journal of Geophysical Research: Solid Earth, 120(9): 6141-6158.

Sparks, R.S.J., Wilson, L. and Sigurdsson, H., 1981. The pyroclastic deposits of the 1875 eruption of Askja, Iceland. Philosophical Transactions of the Royal Society of London. Series A, Mathematical and Physical Sciences, 299(1447): 241-273.

Suñe-Puchol, I., Aguirre-Díaz, G.J., Dávila-Harris, P., Miggins, D.P., Pedrazzi, D., Costa, A., Ortega-Obregón, C., Lacan, P., Hernández, W. and Gutiérrez, E., 2019a. The Ilopango caldera complex, El Salvador: Origin and early ignimbrite-forming eruptions of a graben/pull-apart caldera structure. Journal of Volcanology and Geothermal Research, 371: 1-19.

Suñe-Puchol, I., Aguirre-Díaz, G.J., Pedrazzi, D., Dávila-Harris, P., Miggins, D.P., Costa, A., Ortega-Obregón, C., Lacan, P., Gutierrez, E. and Hernández, W., 2019b. The Ilopango caldera complex, El Salvador: Stratigraphic revision of the complete eruptive sequence and recurrence of large explosive eruptions. Journal of Volcanology and Geothermal Research.

Taddeucci, J., Valentine, G.A., Sonder, I., White, J.D.L., Ross, P.S. and Scarlato, P., 2013. The effect of pre‐existing craters on the initial development of explosive volcanic eruptions: An experimental investigation. Geophysical Research Letters, 40(3): 507-510.

Turner Henry, L., LaFemina, P., Saballos, A., Mattioli Glen, S., Jansma Pamela, E. and Dixon, T., 2007. Kinematics of the Nicaraguan forearc from GPS geodesy. Geophysical Research Letters, 34(2).

Valentine, G.A., Graettinger, A.H., Macorps, É., Ross, P.-S., White, J.D.L., Döhring, E. and Sonder, I., 2015. Experiments with vertically and laterally migrating subsurface explosions with applications to the geology of phreatomagmatic and hydrothermal explosion craters and diatremes. Bulletin of Volcanology, 77(3): 15.

Valentine, G.A., Graettinger, A.H. and Sonder, I., 2014. Explosion depths for phreatomagmatic eruptions. Geophysical Research Letters, 41(9): 3045-3051.

Valentine, G.A. and White, J.D.L., 2012. Revised conceptual model for maar-diatremes: Subsurface processes, energetics, and eruptive products. Geology, 40(12): 1111-1114.

Vallance, J. and Houghton, B., 1998. The AD 260 eruption at Lake Ilopango, El Salvador: A complex explosive eruption through a caldera lake. National Science Foundation, Research Proposal.

Weber, H.S., Wiesemann, G. and Wittekindt, H., 1974. Mapa Geológico de la República de El Salvador / Geologische Übersichtskarte der Republik El Salvador 1 : 500,000 (after geological maps 1:100000 – 1967-74) Bundesanstalt für Geowissenschaften und Rohstoffe, Hannover ; Bundesanstalt fu¨r Bodenforschung, Hannover.

White, J.D.L. and Houghton, B.F., 2006. Primary volcaniclastic rocks. Geology, 34(8): 677-680.

Wilkie, J.W. and Guadalupe Ortega, J., 1997 Statistical Abstracts of LatinAmerica. 33, The Regents of the University of California, Los Angeles.

Willcock, M.A.W., Cas, R.A.F., Giordano, G. and Morelli, C., 2013. The eruption, pyroclastic flow behaviour, and caldera in-filling processes of the extremely large volume (>1290km3), intra- to extra-caldera, Permian Ora (Ignimbrite) Formation, Southern Alps, Italy. Journal of Volcanology and Geothermal Research, 265: 102-126.

Williams, H. and Meyer-Abich, H., 1955. Volcanism in the Southern Part of El Salvador: With Particular Reference to the Collapse Basins of Lakes Coatepeque and Ilopango. University of California Press.

Figure Captions

Fig. 1: a) Geological setting of northern Central America; ESFZ: El Salvador Fault Zone; GF: Gulf of Fonseca; IG: Ipala Graben; JF: Jalpatagua Fault; ND: Nicaraguan Depression; PF: Polochic fault; b) simplified geological map showing all the major geological formations of El Salvador (Hernández, 2004). CC: Coatepeque Caldera; CG: Cerrón Grande dump; I: Izalco Volcano; IC: Ilopango Caldera; LO: Laguna Olomega; SA: Santa Ana Volcano; SM: San Miguel Volcano; SS: San Salvador Volcano; SV: San Vicente Volcano; c) Google Earth image of Ilopango caldera (IC) (US Depth of State Geographer 2018); SSMA: San Salvador Metropolitan area; IQ: Islas Quemadas.

Fig. 2: Stratigraphic logs of TBJ succession of deposits and their locations. Granulometric analysis and lithics content are shown as well. The TBJ eruption can be divided in 8 units from base to top ; Units A_0 to G. Stratigraphic logs are arranged from west (left) to east (right) and from south to north, and cover most of the El Salvador. Inset figure show the locations of the outcrops and samples of Figs. 2 and 3.

Fig. 3: Field photographs of the TBJ units with views of details. a) Units A_0-D resting on a paleosol, see the scraper for scale; b) features of Units A_0 and A: the former is characterized by poorly-sorted thinly, laminated beds of rounded pumice lapilli and coarse ash, and the latter by lithic-rich, massive, well-sorted thin to medium coarse angular pumice ash beds; c) Unit B, it shows massive thin beds of angular pumice lapilli with no ash; d) Units D, E, F. Unit D is an ash rich deposit whilst Unit F is characterized by a coarse ash matrix with abundant centimeter- and decimeter-size pumice and lithic fragments. Unit E has laminated beds; e) photographs of Unit D showing ei) ash matrix and dispersed pumice juvenile fragments with slight variations

between one horizon and another and eii) strong enrichment of millimeter-size accretionary lapilli. Photographs of the characteristics feature of Unit E, f) doublets of thin to medium thick massive and laminated beds lapilli and coarse ash pumice; g) soft-sediments deformation structures: folding; Unit F with h) coarse ash matrix with abundant centimeter-size and decimeter-size pumice and lithic fragments at proximal outcrops, in the inset figure a mingled pumice is shown as well i) chaotic massive poorly-sorted, non-welded, light-colored deposits; j) some decimeter-size lithic-rich levels; k) at distal outcrop; l) degassing pipes; m) reworked (RW) lower part of Unit F; n) Unit G, unconsolidated massive ash deposits with dispersed accretionary lapilli (AL); o) distal outcrops of Unit G reach thicknesses of 40-50 cm at Tazumal Archaeological Site (Chalchuapa). Outcrops numbers are shown in yellow in the inset in Fig. 2. Yellow dotted lines divide different units of the TBJ Member. White dotted lines outline details of the field picture.

Fig. 4: Total Grain Size Distributions of fallout units (A, B and G). For the sake of comparison TGSDs associated to the co-ignimbrite phase of the Campanian Ignimbrite are also reported (Marti et al., 2016).

Fig. 5: Distribution maps of each unit of TBJ eruption: a) Unit A, b) Unit B, C) Unit C, d) Unit D, E) Unit E, F) Unit F, g) and gi) Unit G.

Fig. 6: Petrographic features of the TBJ eruption products: parallel and crossed polarized nichols: a) and b) mineralogy assemblage with euhedral to subhedral plagioclase and hornblende with apatite inclusions; c) and d) detailed picture of plagioclase with pyroxene and oxide inclusions; e) and f) euhedral hornblende; g) and h) subhedral pyroxene with apatite inclusions.

Fig. 7: Microprobe data of a) feldspars (classification of Smith and Brown, 1988); b) amphiboles (classification of Leake et. al., 1997) and c) sodium and d) calcium, magnesium, iron pyroxenes (classification of Morimoto et al. 1989) diagrams.

Fig. 8: a) Plot of TBJ juvenile samples (i.e. pumice clasts) and mingled pumices in the TAS (SiO_2-Na_2O+K_2O) classification diagram of Le Bas et al. (1986). Glass compositions from the entire composition succession of deposits, and from both proximal and distal sites: b) CaO vs FeO; c) and d) SiO_2 vs Al_2O_3

Fig. 9: Sketch (not to scale) illustrating the evolution of the TBJ eruption: a) rise of magma and interaction with a shallow aquifer or water lake and formation of the directional dilute PDCs that spread mainly southward (Unit A_0); fallout phases represented by b) hydromagmatic Unit A and c) magmatic Unit B; d) PDCs of

hydromagmatic origin, due to a renewed magma-water interaction, with formations of Unit C and Unit D; e) PDCs and fallout deposits from the transitional Unit E due to the alternation of dry and wet phases; f) main phase of the TBJ eruption with deposition of Unit F by dense PDCs associated to the caldera collapse; g) co-ignimbrite deposits.

Tables Caption

Table 1: Summary of the physical parameters of the deposits from the TBJ eruption.

Table 2: Whole rock analyses of representative TBJ samples.

Table 3: Representative glass analyses of the TBJ eruption units.

Supplementary Material

Supplementary Material 1: Thickness and location of units from TBJ eruption.

Supplementary Material 2: Grain Size analysis of TBJ deposits.

Supplementary Material 3: Granulometric parameters of TBJ eruption.

Supplementary Material 4: Plots of grain-size data from TBJ deposits. (a-c) Sorting ($\sigma\Phi$) v. median diameter ($Md\Phi$); (d-f) sorting ($\sigma\Phi$) vs. skewness ($\alpha\Phi$); (g-i) F1 (wt.% <1 mm diameter) versus F2 (wt.% <1/16 mm diameter); (j-ac) granulometric frequency distribution.

Supplementary Material 5: Modal proportions of juvenile pumice and accidental lithic fragments.

Supplementary Material 6: Electron microprobe analysis of TBJ minerals

Supplementary Material 7: Electron microprobe analysis of TBJ glass

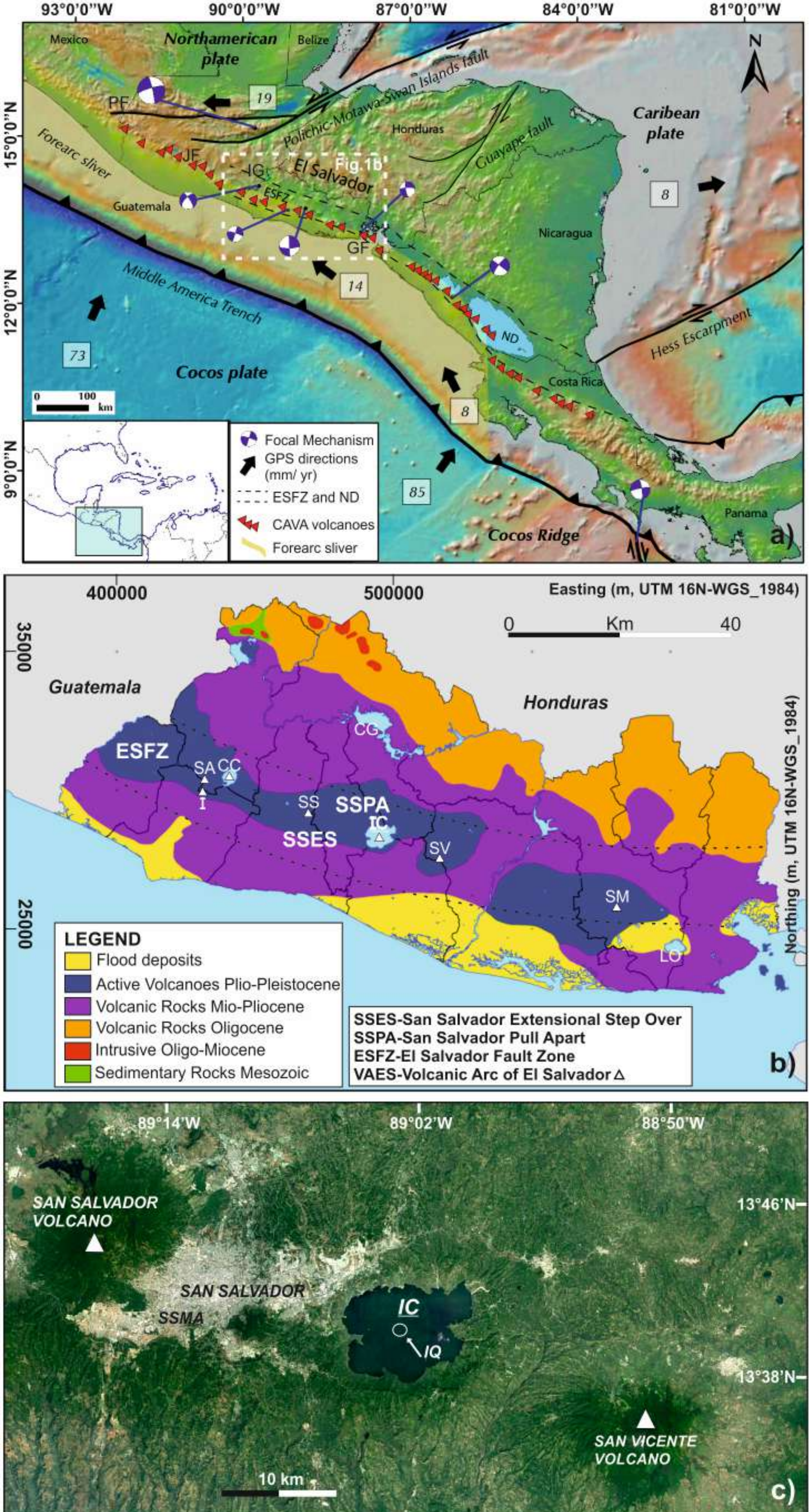
93°0'0"W
90°0'0"W
87°0'0"W
84°0'0"W
81°0'0"W
15°0'0"N
12°0'0"N
9°0'0"N
Mexico
Northamerican plate
Belize
19
PF
Polichic-Motawa-Swan Islands fault
Honduras
Guayape fault
Caribean plate
Forearc sliver
JF
IG
Fig.1b
El Salvador
ESFZ
Guatemala
8
Nicaragua
GF
14
Middle America Trench
ND
Hess Escarpment
73
Cocos plate
Costa Rica
0
100
km
8
Focal Mechanism
GPS directions (mm/ yr)
ESFZ and ND
CAVA volcanoes
Forearc sliver
85
Panama
Cocos Ridge
a)
400000
500000
Easting (m, UTM 16N-WGS_1984)
0
Km
40
35000
Guatemala
Honduras
CG
ESFZ
SA
CC
I
SS
SSPA
IC
SSES
SV
Northing (m, UTM 16N-WGS_1984)
25000
SM
LO
LEGEND
Flood deposits
Active Volcanoes Plio-Pleistocene
Volcanic Rocks Mio-Pliocene
Volcanic Rocks Oligocene
Intrusive Oligo-Miocene
Sedimentary Rocks Mesozoic
SSES-San Salvador Extensional Step Over
SSPA-San Salvador Pull Apart
ESFZ-El Salvador Fault Zone
VAES-Volcanic Arc of El Salvador △
b)
89°14'W
89°02'W
88°50'W
13°46'N
13°38'N
SAN SALVADOR VOLCANO
SAN SALVADOR
SSMA
IC
IQ
SAN VICENTE VOLCANO
10 km
c)

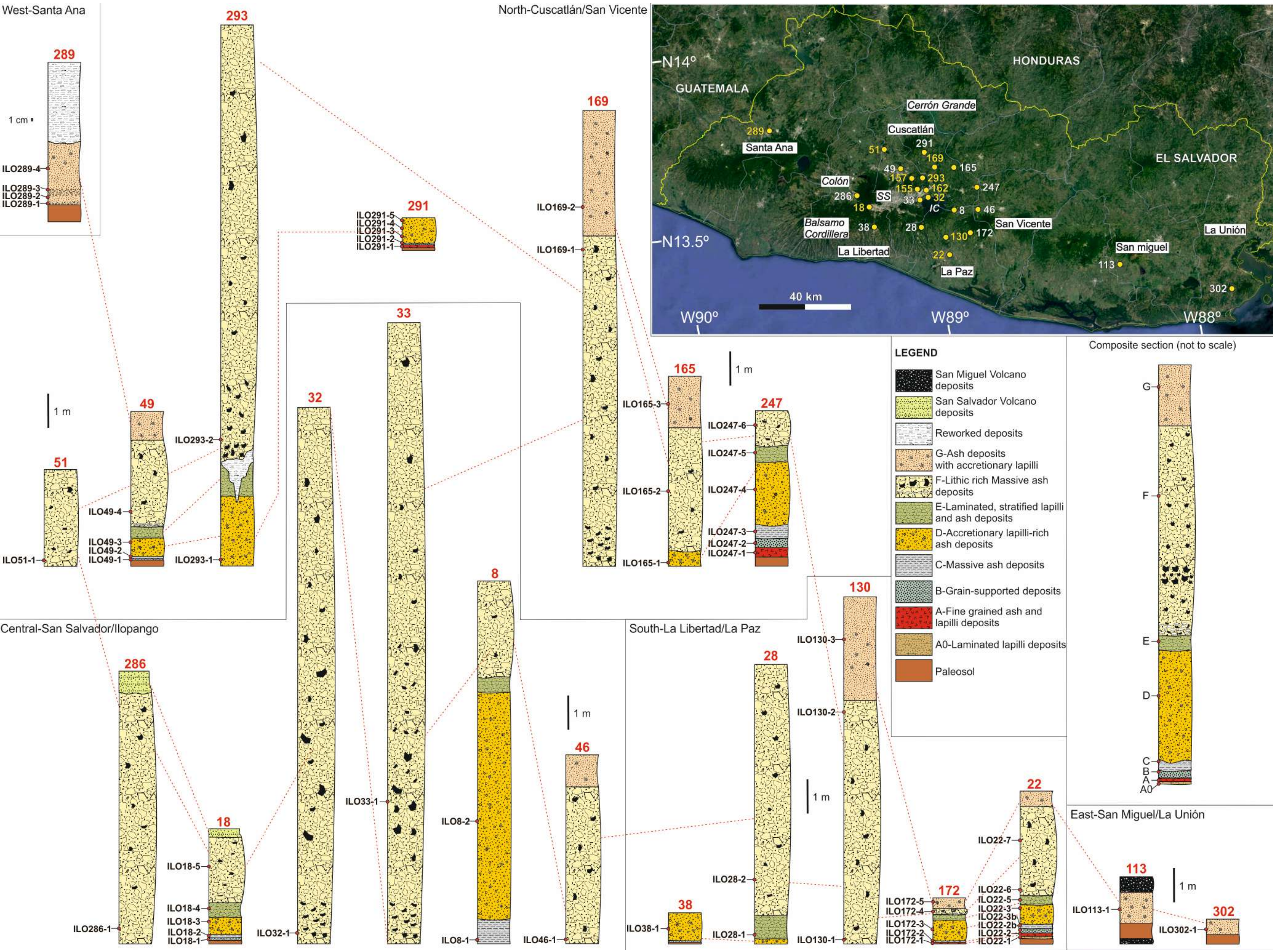
West-Santa Ana
289
1 cm
ILO289-4
ILO289-3
ILO289-2
ILO289-1
293
ILO293-2
ILO293-1
291
ILO291-5
ILO291-4
ILO291-3
ILO291-2
ILO291-1
1 m
51
ILO51-1
49
ILO49-4
ILO49-3
ILO49-2
ILO49-1
North-Cuscatlán/San Vicente
169
ILO169-2
ILO169-1
165
ILO165-3
ILO165-2
ILO165-1
1 m
247
ILO247-6
ILO247-5
ILO247-4
ILO247-3
ILO247-2
ILO247-1
GUATEMALA
HONDURAS
EL SALVADOR
N14º
N13.5º
W90º
W89º
W88º
Cerrón Grande
Cuscatlán
Santa Ana
Colón
SS
IC
Balsamo Cordillera
La Libertad
La Paz
San Vicente
San miguel
La Unión
40 km
289
51
291
169
165
49
157
293
155
162
247
286
33
32
18
8
46
38
28
130
172
22
113
302
LEGEND
San Miguel Volcano deposits
San Salvador Volcano deposits
Reworked deposits
G-Ash deposits with accretionary lapilli
F-Lithic rich Massive ash deposits
E-Laminated, stratified lapilli and ash deposits
D-Accretionary lapilli-rich ash deposits
C-Massive ash deposits
B-Grain-supported deposits
A-Fine grained ash and lapilli deposits
A0-Laminated lapilli deposits
Paleosol
Composite section (not to scale)
G
F
E
D
C
B
A
A0
Central-San Salvador/Ilopango
286
ILO286-1
18
ILO18-5
ILO18-4
ILO18-3
ILO18-2
ILO18-1
32
ILO32-1
33
ILO33-1
8
ILO8-2
ILO8-1
1 m
46
ILO46-1
South-La Libertad/La Paz
38
ILO38-1
28
ILO28-2
ILO28-1
130
ILO130-3
ILO130-2
ILO130-1
1 m
172
ILO172-5
ILO172-4
ILO172-3
ILO172-2
ILO172-1
22
ILO22-7
ILO22-6
ILO22-5
ILO22-3
ILO22-3b
ILO22-2b
ILO22-2
ILO22-1
East-San Miguel/La Unión
113
ILO113-1
1 m
302
ILO302-1

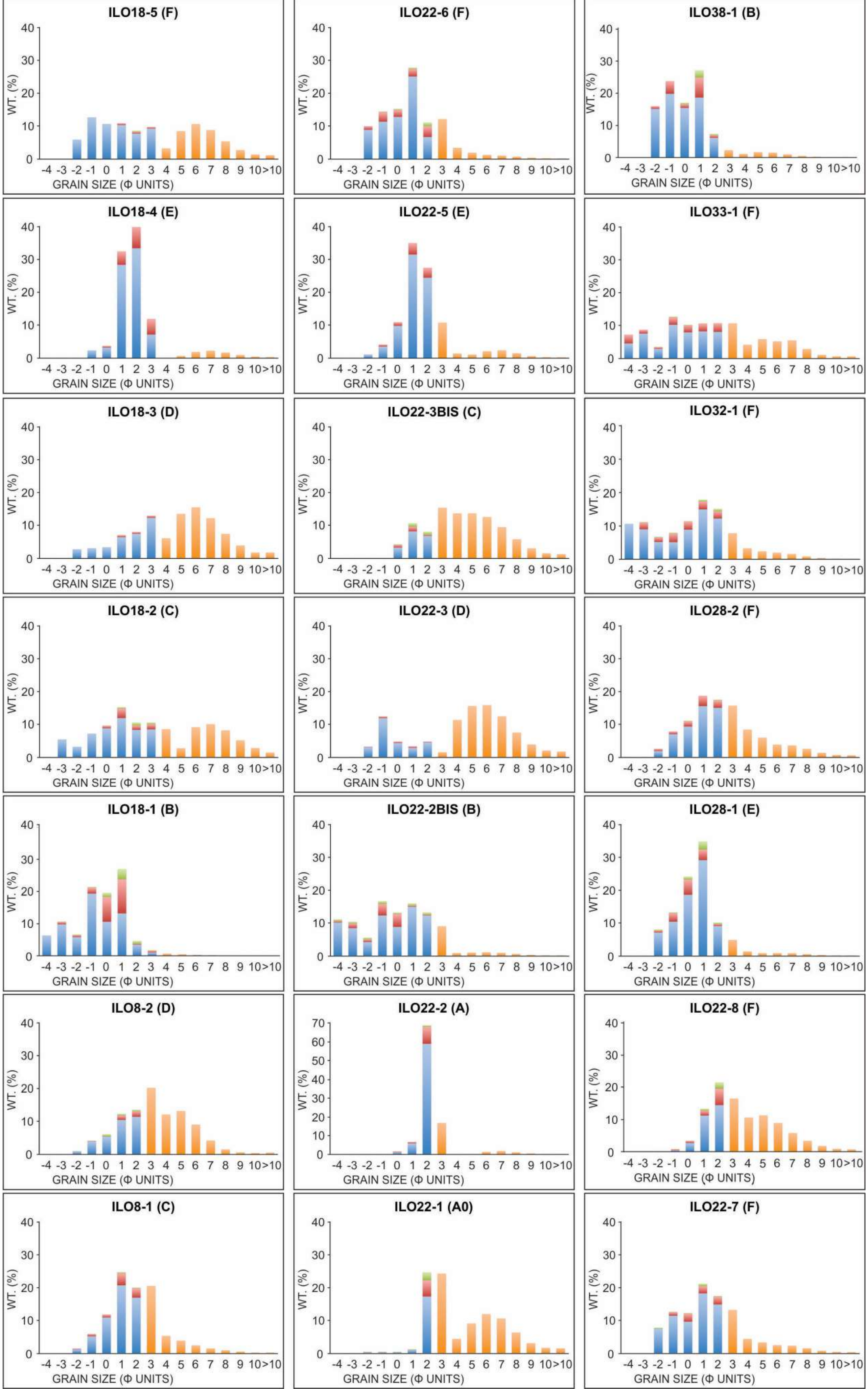
ILO18-5 (F)
ILO22-6 (F)
ILO38-1 (B)
ILO18-4 (E)
ILO22-5 (E)
ILO33-1 (F)
ILO18-3 (D)
ILO22-3BIS (C)
ILO32-1 (F)
ILO18-2 (C)
ILO22-3 (D)
ILO28-2 (F)
ILO18-1 (B)
ILO22-2BIS (B)
ILO28-1 (E)
ILO8-2 (D)
ILO22-2 (A)
ILO22-8 (F)
ILO8-1 (C)
ILO22-1 (A0)
ILO22-7 (F)
WT. (%)
GRAIN SIZE (Φ UNITS)
-4 -3 -2 -1 0 1 2 3 4 5 6 7 8 9 10 >10

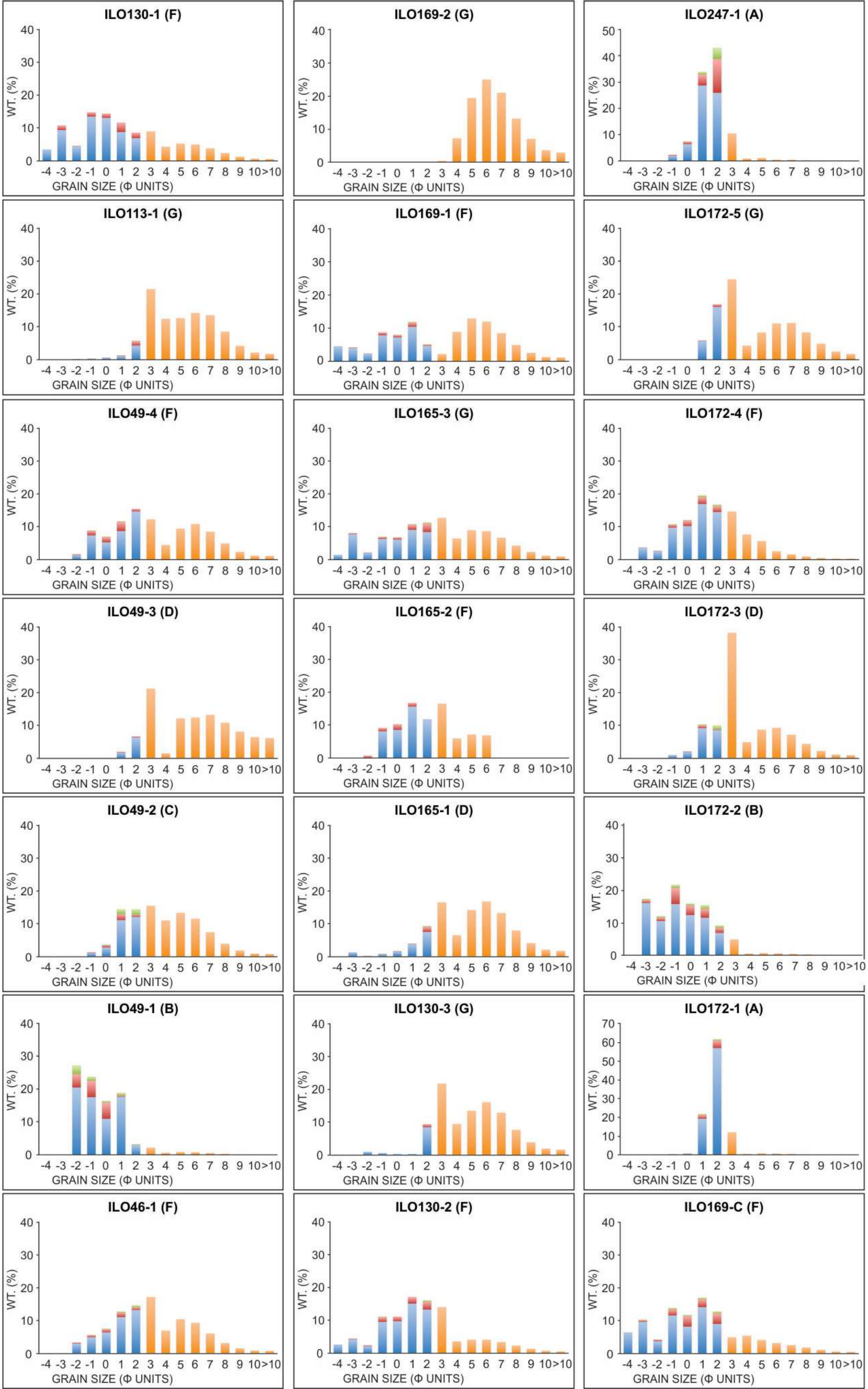
ILO130-1 (F)
ILO169-2 (G)
ILO247-1 (A)
ILO113-1 (G)
ILO169-1 (F)
ILO172-5 (G)
ILO49-4 (F)
ILO165-3 (G)
ILO172-4 (F)
ILO49-3 (D)
ILO165-2 (F)
ILO172-3 (D)
ILO49-2 (C)
ILO165-1 (D)
ILO172-2 (B)
ILO49-1 (B)
ILO130-3 (G)
ILO172-1 (A)
ILO46-1 (F)
ILO130-2 (F)
ILO169-C (F)
WT. (%)
GRAIN SIZE (Φ UNITS)

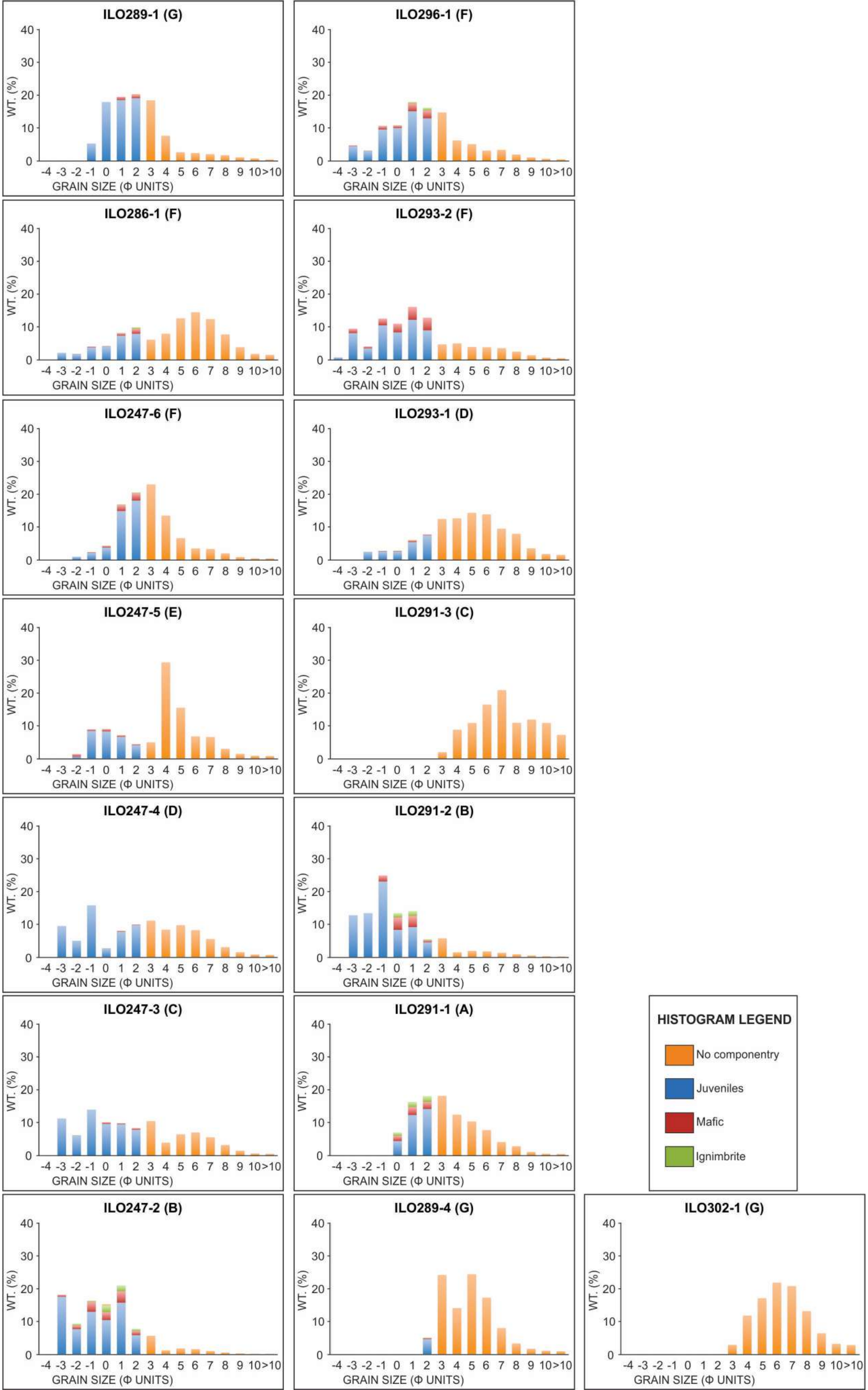
ILO289-1 (G)
ILO296-1 (F)
ILO286-1 (F)
ILO293-2 (F)
ILO247-6 (F)
ILO293-1 (D)
ILO247-5 (E)
ILO291-3 (C)
ILO247-4 (D)
ILO291-2 (B)
ILO247-3 (C)
ILO291-1 (A)
ILO247-2 (B)
ILO289-4 (G)
ILO302-1 (G)
WT. (%)
GRAIN SIZE (Φ UNITS)
HISTOGRAM LEGEND
No componentry
Juveniles
Mafic
Ignimbrite

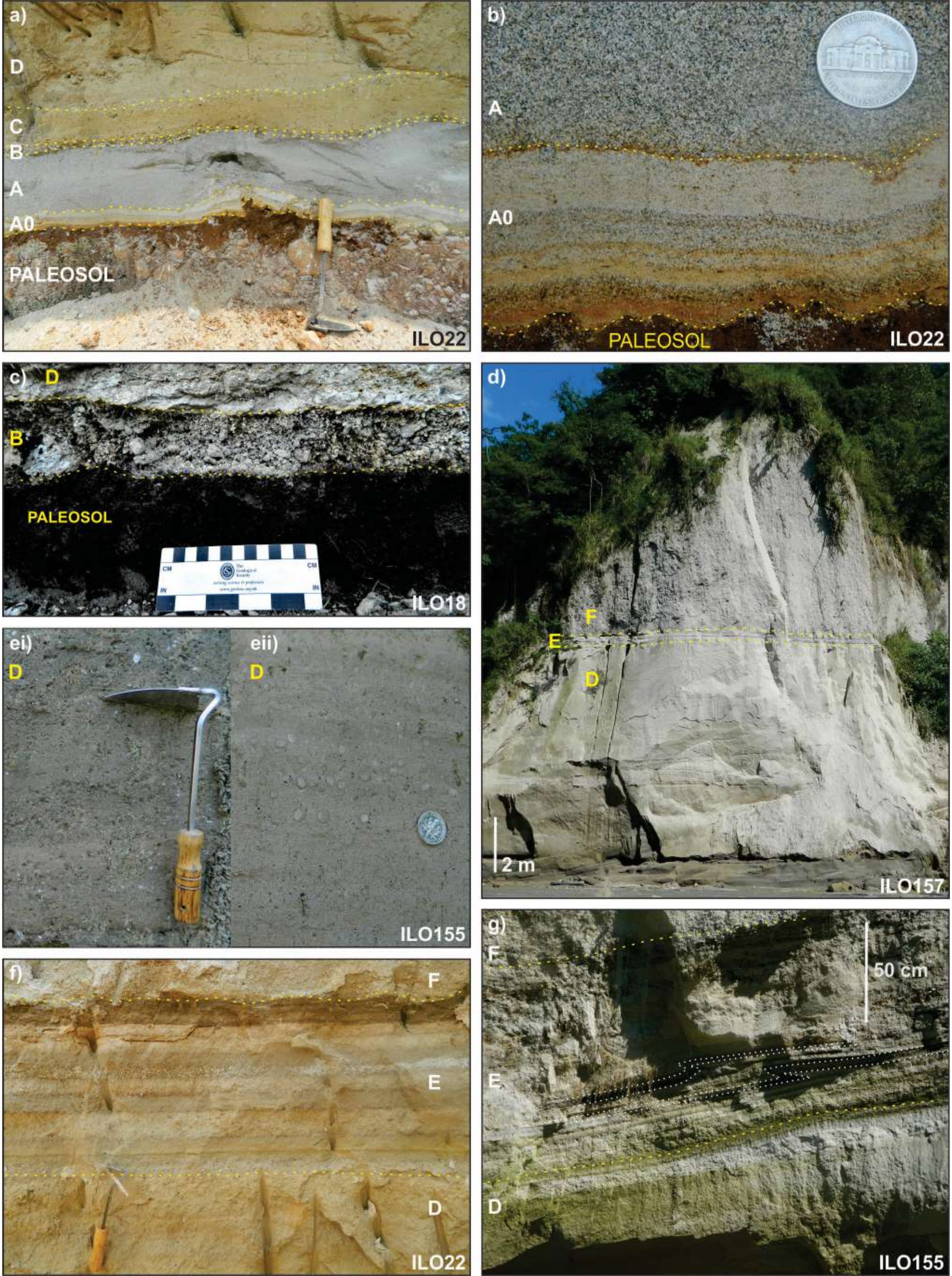
a)
D
C
B
A
A0
PALEOSOL
ILO22
b)
A
A0
PALEOSOL
ILO22
c)
D
B
PALEOSOL
ILO18
d)
F
E
D
2 m
ILO157
ei)
D
eii)
D
ILO155
f)
F
E
D
ILO22
g)
F
50 cm
E
D
ILO155


h)
F
CM
IN
CM
IN
ILO32
i)
F
ILO169
j)
F
50 cm
F
ALTO
ILO162
k)
F
ILO51
l)
F
50 cm
ILO155
m)
F
RW
D
ILO293
n)
AL
ILO130
o)
40 cm
G
ILO289

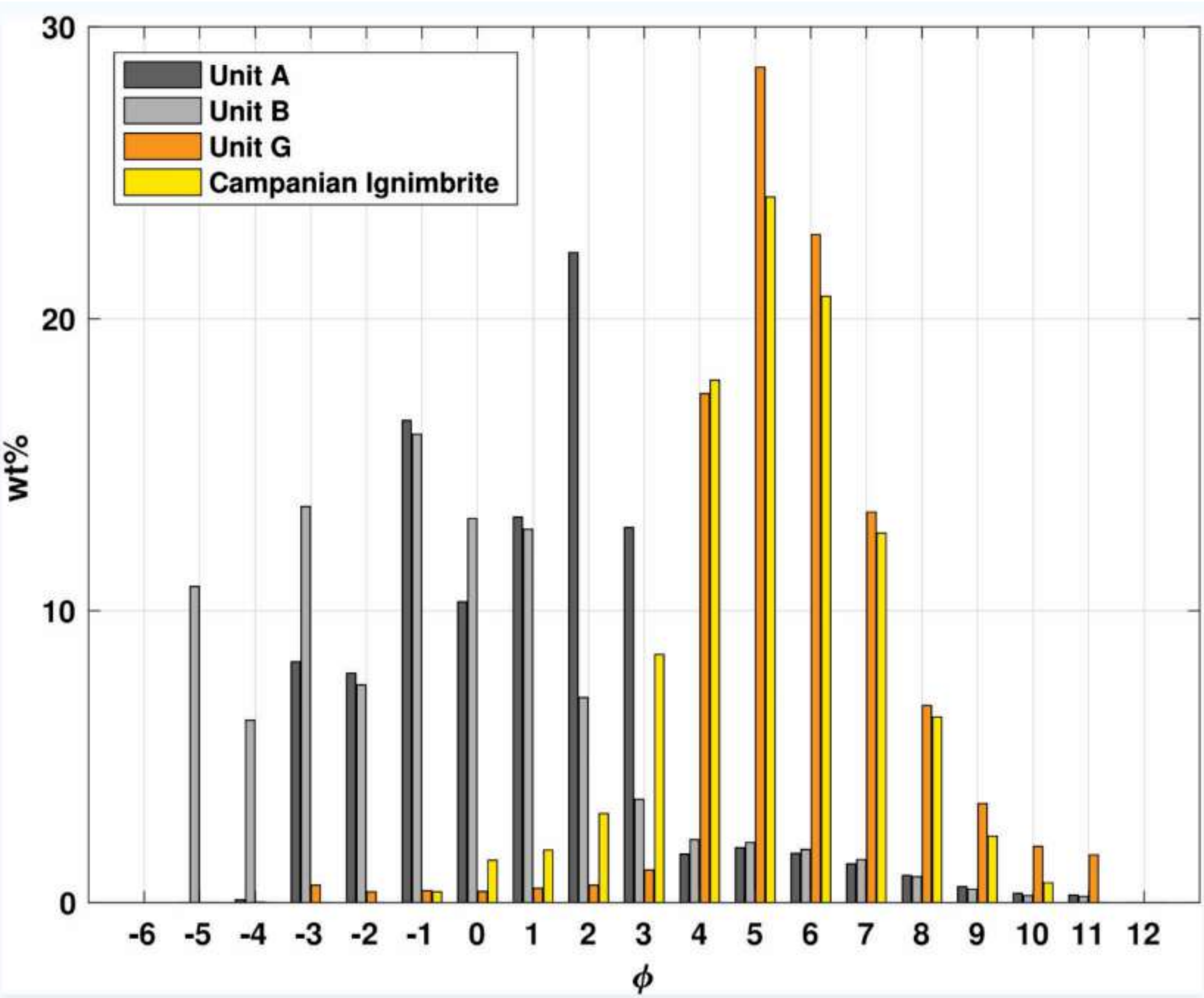

Unit A
Unit B
Unit G
Campanian Ignimbrite
wt%
30
20
10
0
-6
-5
-4
-3
-2
-1
0
1
2
3
4
5
6
7
8
9
10
11
12
ϕ

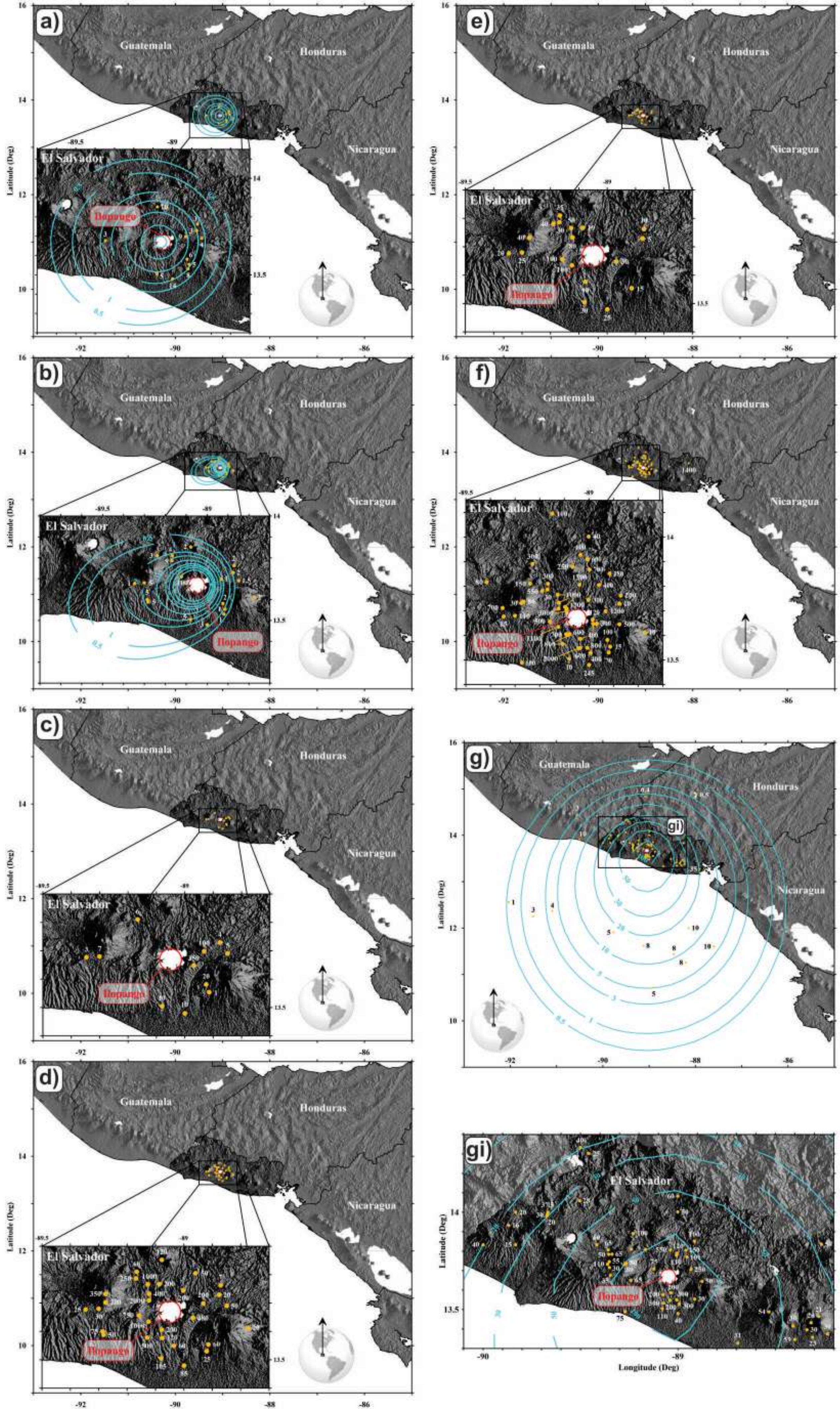
a)
b)
c)
d)
e)
f)
g)
gi)
Guatemala
Honduras
Nicaragua
El Salvador
Ilopango
Latitude (Deg)
Longitude (Deg)

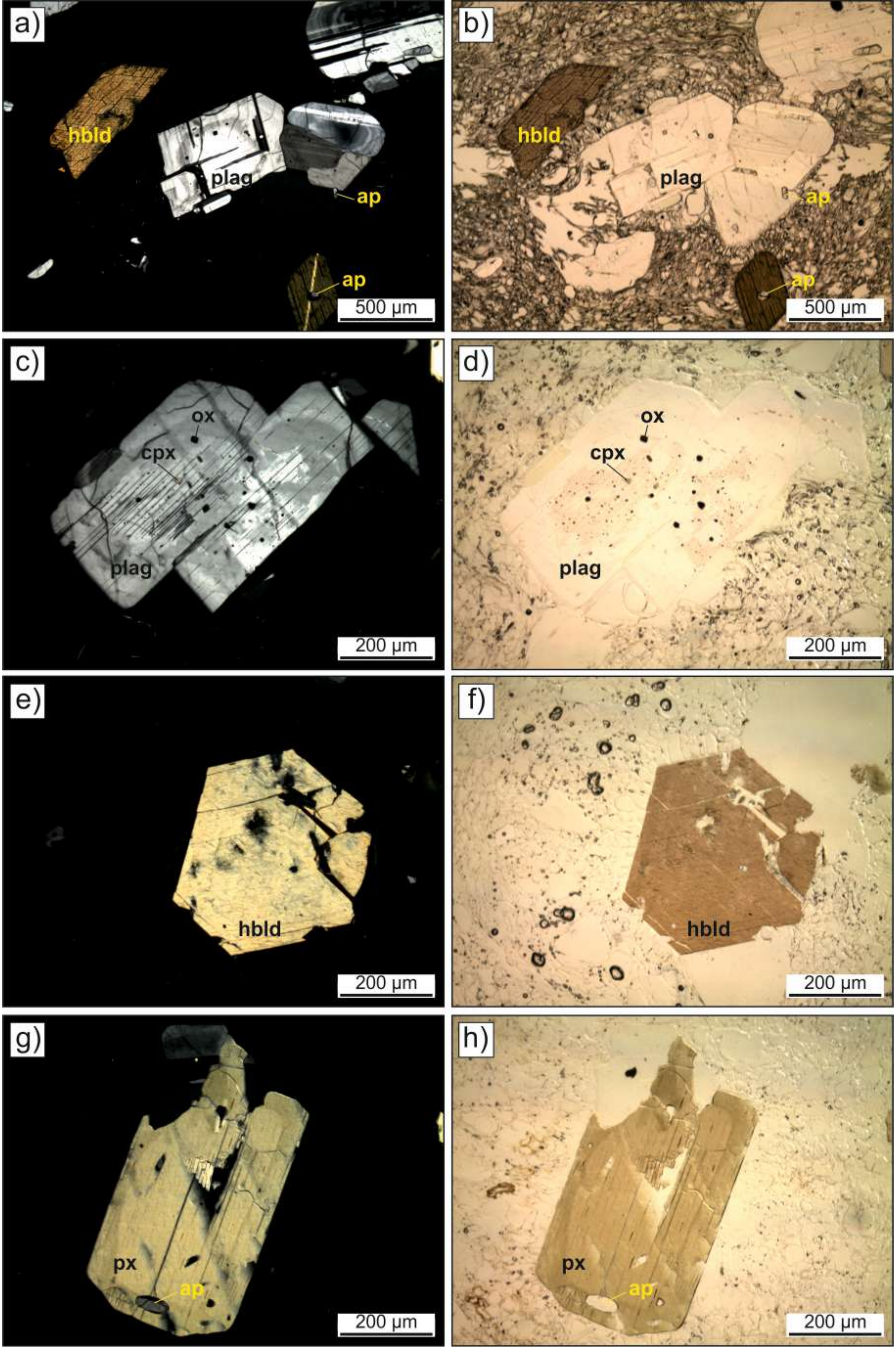
a)
hbld
plag
ap
ap
500 µm
b)
hbld
plag
ap
ap
500 µm
c)
ox
cpx
plag
200 µm
d)
ox
cpx
plag
200 µm
e)
hbld
200 µm
f)
hbld
200 µm
g)
px
ap
200 µm
h)
px
ap
200 µm

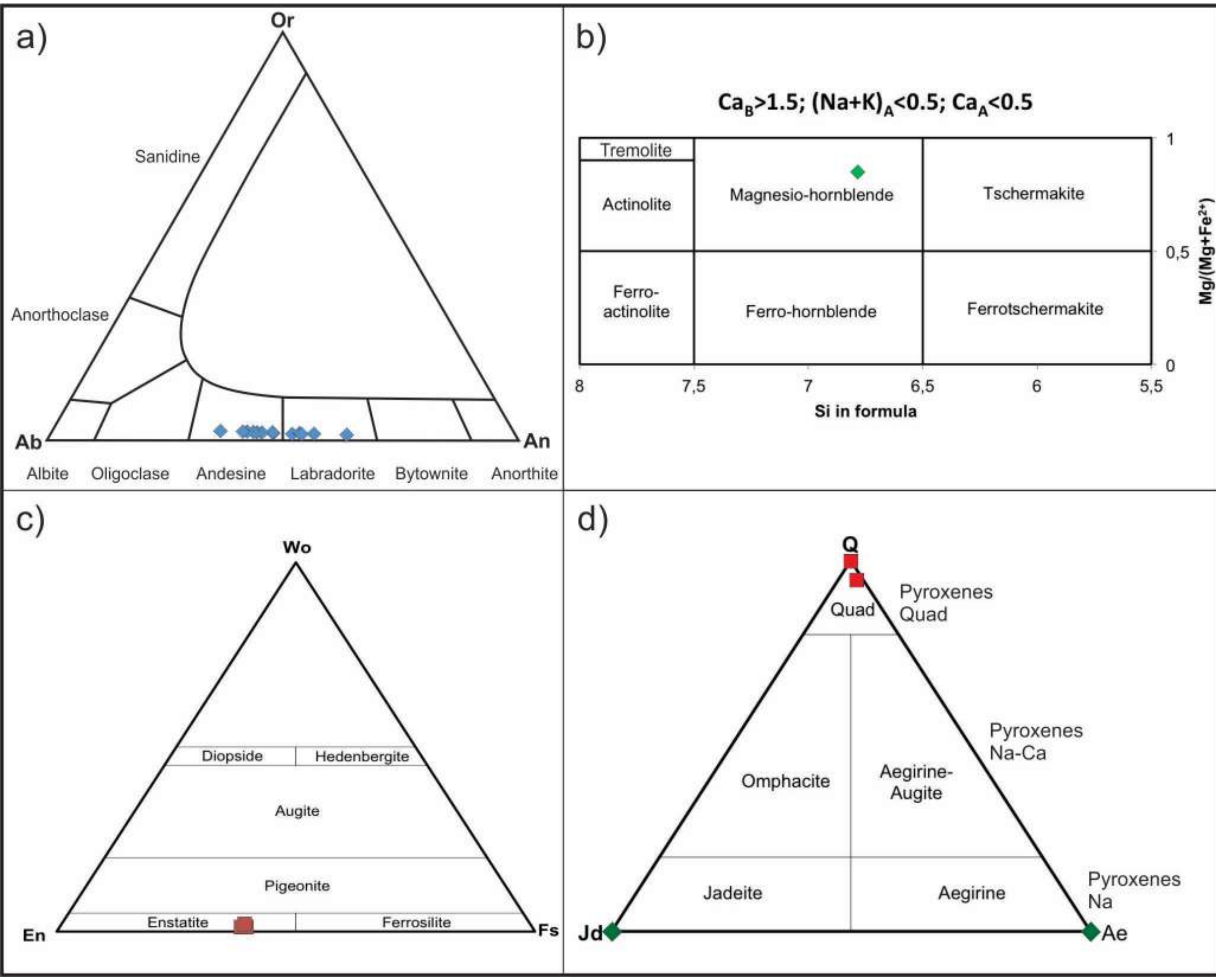
a)
Or
Sanidine
Anorthoclase
Ab
An
Albite
Oligoclase
Andesine
Labradorite
Bytownite
Anorthite
b)
Ca_B>1.5; $(Na+K)_A$<0.5; Ca_A<0.5
Tremolite
Actinolite
Magnesio-hornblende
Tschermakite
Ferro-actinolite
Ferro-hornblende
Ferrotschermakite
$Mg/(Mg+Fe^{2+})$
1
0,5
0
8
7,5
7
6,5
6
5,5
Si in formula
c)
Wo
Diopside
Hedenbergite
Augite
Pigeonite
Enstatite
Ferrosilite
En
Fs
d)
Q
Quad
Pyroxenes Quad
Pyroxenes Na-Ca
Omphacite
Aegirine-Augite
Jadeite
Aegirine
Pyroxenes Na
Jd
Ae

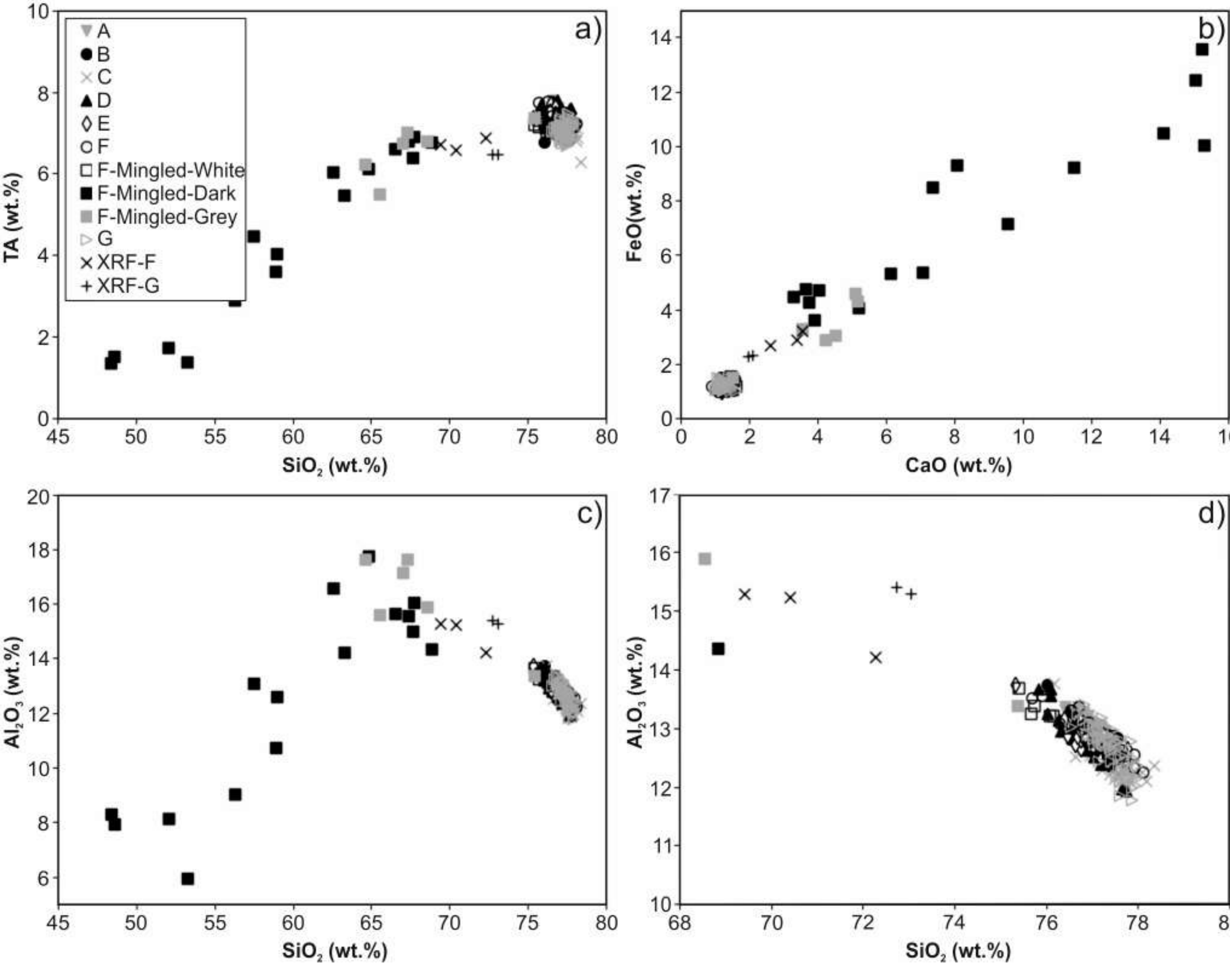

a)
b)
c)
d)
A
B
C
D
E
F
F-Mingled-White
F-Mingled-Dark
F-Mingled-Grey
G
XRF-F
XRF-G
TA (wt.%)
SiO2 (wt.%)
FeO(wt.%)
CaO (wt.%)
Al2O3 (wt.%)
SiO2 (wt.%)
Al2O3 (wt.%)
SiO2 (wt.%)

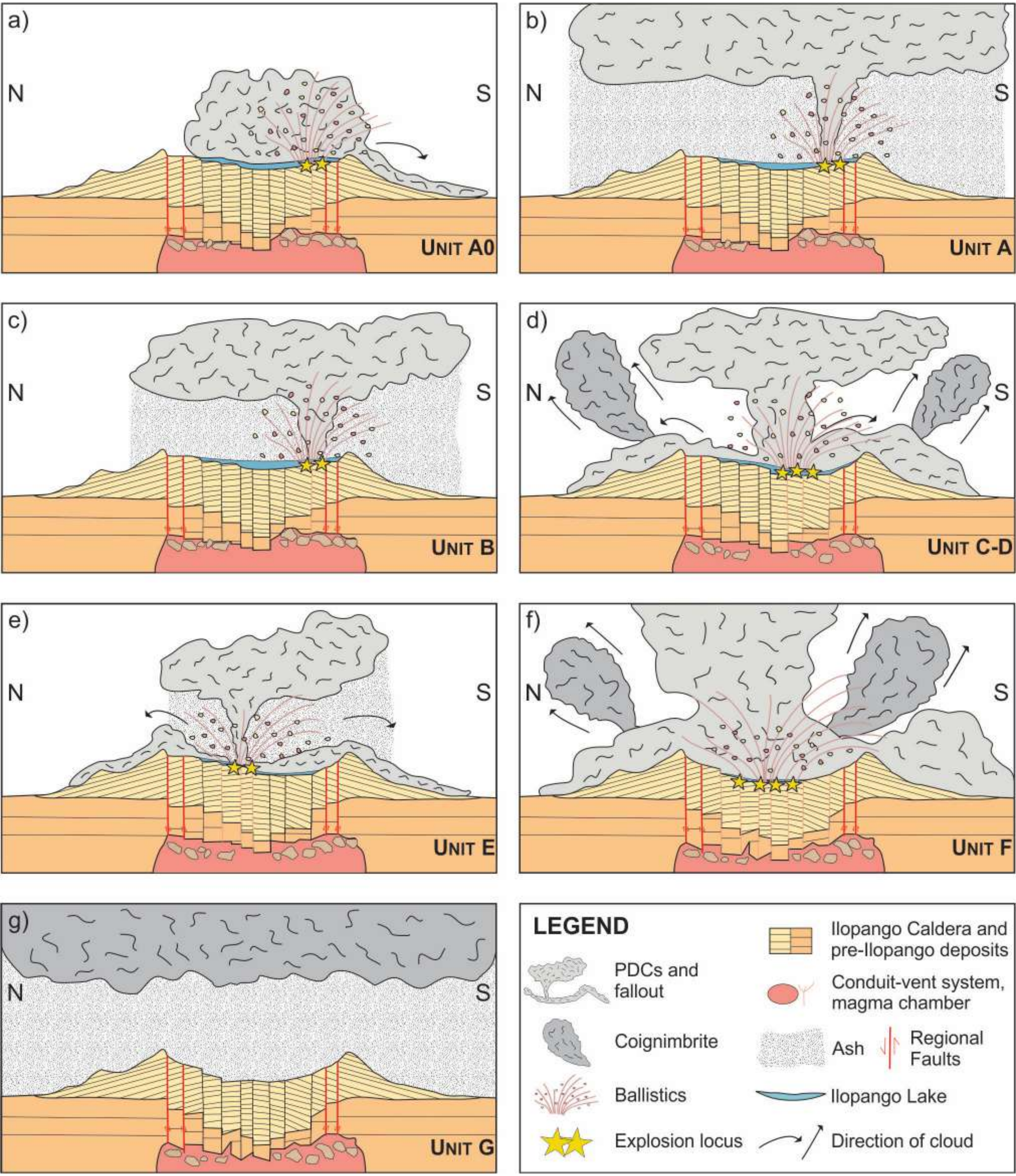
a)
N
S
UNIT A0
b)
N
S
UNIT A
c)
N
S
UNIT B
d)
N
S
UNIT C-D
e)
N
S
UNIT E
f)
N
S
UNIT F
g)
N
S
UNIT G
LEGEND
PDCs and fallout
Coignimbrite
Ballistics
Explosion locus
Ilopango Caldera and pre-Ilopango deposits
Conduit-vent system, magma chamber
Ash
Regional Faults
Ilopango Lake
Direction of cloud

Tab. 1 Summary of the physical parameters of the deposits from the TBJ eruption

Physical parameters	Unit A0	Unit A	Unit B	Unit C	Unit D	Unit E	Unit F	Unit G	Total TBJ	
Bulk Volume (km^3)	<0.1	0.35	1.84	0.7	5	0.5	14	36.80	69.35	"+ caldera filling"
Total Erupted Mass (kg)	<0.1	3.5×10^{11}	2×10^{12}	1.2×10^{12}	8.2×10^{12}	0.7×10^{12}	2.3×10^{13}	4×10^{13}	7.5×10^{13}	"+ caldera filling"
DRE volume (km^3)	<0.1	0.15	0,8	0.5	3.3	0.3	9.1	16	30	"+ caldera filling"
Mass Eruption Rate (kg/s)	$\sim10^{9}$	$\sim10^{8}$	$\sim 10^{5}$-10^{6}	$\sim10^{9}$	$\sim10^{9}$	$\sim10^{9}$	$\sim10^{10}$	$\sim10^{10}$	-	
Runout PDC (km)	20	-	-	25	25	20	50	-	-	
Column Height (km)	-	29	7	-	-	-	-	49	-	
Magnitude	-	-	-	-	-	-	-	-	6.8	

Table 2 Whole rock analyses of representative TBJ samples

Sample	ILO-32-2	ILO-128-1	ILO-169-A	ILO-302-1	ILO-303-1
TBJ Unit	F (base)	F (base)	F (Base)	G	G
Site	Apulo	S. Anton. Masahuat	Oratorio	La Union	Santa Elena
Distance	Proximal	Medial	Medial	Distal	Distal
Latitude	N13°42.504'	N13°32.826'	N13°48.382'	N13°16.263'	N13°24.965'
Longitude	W89°05.365'	W89°02.510'	W89°02.301'	W87°54.421'	W88°24.560'
Major and minor elements (oxides, wt.%)					
SiO2	67,34	70,325	68,631	70,45	70,081
TiO2	0,408	0,301	0,34	0,247	0,25
Al2O3	14,833	13,826	14,846	14,744	14,835
Fe2O3	3,475	2,913	3,142	2,431	2,495
MnO	0,122	0,109	0,113	0,099	0,101
MgO	1,216	0,873	0,995	0,557	0,597
CaO	3,453	2,528	3,311	1,9	2,01
Na2O	4,317	4,263	4,295	3,623	3,64
K2O)	2,188	2,433	2,122	2,621	2,595
P2O5	0,133	0,097	0,105	0,06	0,067
Total	99,975	99,888	99,99	99,932	99,891
LOI	2,49	2,22	2,09	3,2	3,22
Trace elements (ppm)					
Li	14	15	8	20	20
Be	1	1	1	1	1
B	43	73	41	39	31
P	0	0	0	0	0
Sc	5	3	7	2	3
Ti	0	0	0	0	0
V	40	27	34	20	22
Cr	3	3	3	3	3
Co	5	4	4	3	4
Ni	2	2	3	2	2
Cu	9	6	8	14	16
Zn	47	44	44	40	41
Ga	14	13	13	14	14
Rb	37	48	27	56	55
Sr	308	242	284	191	213
Y	17	17	15	17	17
Zr	144	149	149	139	143
Nb	3	4	3	4	4
Mo	2	2	2	2	2
Sn	1	1	1	3	3
Sb	1	1	1	1	1
Cs	2	2	2	3	3
Ba	997	1111	974	1271	1199
La	12	13	10	14	13
Ce	24	26	19	28	28
Pr	3	3	3	3	3
Nd	13	13	11	13	13
Sm	3	3	2	3	3
Eu	1	1	1	1	1
Tb	0	0	0	0	0
Gd	3	3	2	3	3
Dy	3	3	2	3	3
Ho	1	1	1	1	1
Er	2	2	2	2	2
Yb	2	2	2	2	2
Lu	0	0	0	0	0
Hf	4	4	4	4	4
Ta	0	0	0	0	0
W	0	1	0	1	1
Tl	0	0	0	0	0
Pb	6	7	6	8	8
Th	3	3	2	4	4
U	1	2	1	2	2

Samples analyzed by X-Ray Fluorescence in the Insituto de Geología (UNAM) by Patricia Girón.
Coordinates in WGS84 system (zone 16P).
LOI: Lost of ignition

Table 3 Representative glass analyses of the TBJ eruption units

Sample	ILO-122-1	ILO-122-2	ILO-122-3	ILO-8-1	ILO-122-4	ILO-2-1	ILO-122-6	ILO-8-3	ILO-8-2
TBJ Unit	A (base)	A (top)	B (top)	C	C	D	Da (top)	Db	Dc
Site	Comalapa	Comalapa	Comalapa	E San Emigdio	Comalapa	San Marcos	Comalapa	E San Emigdio	E San Emigdio
Distance	Medial	Medial	Medial	Proximal	Medial	Proximal	Medial	Proximal	Proximal
Latitude	N13°30.283'	N13°30.283'	N13°30.283'	N13°38.876'	N13°30.283'	N13°39.381'	N13°30.283'	N13°38.876'	N13°38.876'
Longitude	W89°04.805'	W89°04.805'	W89°04.805'	W88°58.097'	W89°04.805'	W89°9.517'	W89°04.805'	W88°58.097'	W88°58.097'
Analysis label	ILO-122-1_17	ILO-122-2_13	ILO-122-3_12	TBJ_8-1_6	ILO-122-4_15	TBJ_2-1_8	ILO-122-6_4	TBJ_8-3_16	TBJ_8-2_9
SiO_2	76,42	76,85	77,22	77,31	77,38	77,05	76,79	76,11	77,04
TiO_2	0,19	0,24	0,19	0,17	0,17	0,19	0,17	0,18	0,20
Al_2O_3	13,30	13,09	12,83	12,84	12,64	12,68	13,14	13,66	12,51
FeO	1,23	1,09	1,06	0,99	1,17	1,18	1,10	1,06	1,23
MnO	0,13	0,12	0,12	0,02	0,07	0,11	0,10	0,03	0,05
MgO	0,18	0,22	0,22	0,20	0,23	0,19	0,23	0,19	0,23
CaO	1,38	1,22	1,21	1,23	1,21	1,22	1,27	1,50	1,19
Na_2O	4,30	4,32	4,54	4,44	4,43	4,59	4,34	4,44	4,50
K_2O	2,87	2,84	2,82	2,80	2,71	2,80	2,86	2,81	3,06
P_2O_5				0,01		0,02		0,02	0,02
Cl				0,17		0,19		0,16	0,21
Analytical total	98,08	99,00	97,36	95,65	97,41	96,13	95,01	95,76	96,84

Sample	ILO-8-4	ILO-32	ILO-32	ILO-32	ILO-32	ILO-9-1	ILO-122-9	ILO-289	Average	1s
TBJ Unit	E	F	F-Mingled-White	F-Mingled-Grey	F-Mingled-Dark	F	G	G (distal)		
Site	E San Emigdio	Urb. La Selva	Urb. La Selva	Urb. La Selva	Urb. La Selva	E Ilopango	Comalapa	Tazumal		
Distance	Proximal	Proximal	Proximal	Proximal	Proximal	Proximal	Medial	Distal		
Latitude	N13°38.876'	N13°42.504'	N13°42.504'	N13°42.504'	N13°42.504'	N13°39.807'	N13°30.283'	N13°58.769'		
Longitude	W88°58.097'	W89°05.365'	W89°05.365'	W89°05.365'	W89°05.365'	W88°59.099'	W89°04.805'	W89°40.397'		
Analysis label	TBJ_8-4_19	ILO-32_13	ILO-32_white-4	ILO-32_grey-2	ILO-32_dark-13	TBJ_9-1_13	ILO-122-9_12	ILO-289_6	n=240; P_2O_5 & Cl, n=100	
SiO_2	76,76	78,12	76,16	65,55	52,09	77,58	77,22	77,40	77,07	0,47
TiO_2	0,15	0,16	0,21	0,49	1,17	0.15	0,19	0,19	0,19	0,03
Al_2O_3	13,12	12,24	13,20	15,60	8,12	12,47	12,74	12,80	12,81	0,30
FeO	1,07	1,08	1,19	4,58	10,02	1,00	1,26	1,02	1,19	0,11
MnO	0,05	0,00	0,10	0,20	0,30	0.03	0,09	0,09	0,07	0,05
MgO	0,17	0,16	0,26	2,63	11,14	0,19	0,18	0,18	0,20	0,03
CaO	1,24	1,00	1,60	5,09	15,28	1,14	1,28	1,24	1,23	0,10
Na_2O	4,62	4,26	4,07	3,82	1,24	4,41	4.31	4,36	4,36	0,20
K_2O	2,83	2,97	2,95	1,68	0,50	3.03	2,71	2,72	2,88	0,13
P_2O_5	0,08		0,03	0,17	0,08	0,02			0,03	0,02
Cl	0,17		0,22	0,17	0,05	0,20			0,20	0,02
Analytical total	99,43	97,36	94,46	92,68	97,85	94,78	98,59	99,52		

EPMA of individual glass shards aquired at 15kV and 6 nA using a 10 micron defoccused beam. Data are normalised to 100% to account for variable hydration and facilitate comparision.